The Astrophysical Journal, 884:48 (28pp), 2019 October 10 https://doi.org/10.3847/1538-4357/ab378d

The Seven Most Massive Clumps in W43-Main as Seen by ALMA: Dynamical Equilibrium and Magnetic Fields

Paulo C. Cortes[1,2], Charles L. H. Hull[1,3,16], Josep M. Girart[4,5], Carlos Orquera-Rojas[6,7,8], Tirupati K. Sridharan[9], Zhi-Yun Li[10], Fabien Louvet[11], Juan R. Cortes[1,2], Valentin J. M. Le Gouellec[12,13], Richard M. Crutcher[14], and Shih-Ping Lai[15]
[1] Joint ALMA Office, Alonso de Cordova 3107, Vitacura, Santiago, Chile
[2] National Radio Astronomy Observatory, Charlottesville, VA 22903, USA
[3] National Astronomical Observatory of Japan, NAOJ Chile Observatory, Alonso de Córdova 3788, Office 61B, 7630422, Vitacura, Santiago, Chile
[4] Institut de Ciències de l'Espai (ICE, CSIC), Campus UAB, C/Can Magrans S/N, E-08193 Cerdanyola del Vallès, Catalonia, Spain
[5] Institut d'Estudis Espacials de Catalunya (IEEC), E-08034 Barcelona, Catalonia, Spain
[6] Departamento de Física, Universidad Católica del Norte, Av. Angamos 0610, Antofagasta, Chile
[7] Instituto de Astrofísica, Facultad de Física, Pontificia Universidad Católica de Chile, Santiago, Chile
[8] Millennium Institute of Astrophysics (MAS), Nuncio Monsenor Sótero Sanz 100, Providencia, Santiago, Chile
[9] Harvard-Smithsonian Center for Astrophysics, 60 Garden St., Cambridge, MA 02138, USA
[10] Astronomy Department, University of Virginia, Charlottesville, VA 22904, USA
[11] Departamento de Astronomia—Universidad de Chile, Chile
[12] European Southern Observatory, Alonso de Córdova 3107, Vitacura, Santiago, Chile
[13] AIM, CEA, CNRS, Université Paris-Saclay, Université Paris Diderot, Sorbonne Paris Cité, F-91191 Gif-sur-Yvette, France
[14] Astronomy Department, University of Illinois at Urbana-Champaign, IL 61801, USA
[15] Institute of Astronomy and Department of Physics, National Tsing Hua University, Hsinchu 30013, Taiwan
Received 2019 May 6; revised 2019 July 15; accepted 2019 July 30; published 2019 October 11

Abstract

Here we present new ALMA observations of polarized dust emission from six of the most massive clumps in W43-Main. The clumps MM2, MM3, MM4, MM6, MM7, and MM8, have been resolved into two populations of fragmented filaments. From these two populations we extracted 81 cores (96 with the MM1 cores) with masses between $0.9\,M_{\odot}$ to $425\,M_{\odot}$ and a mass sensitivity of $0.08\,M_{\odot}$. The MM6, MM7, and MM8 clumps show significant fragmentation, but the polarized intensity appears to be sparse and compact. The MM2, MM3, and MM4 population shows less fragmentation, but with a single protostellar core dominating the emission at each clump. Also, the polarized intensity is more extended and significantly stronger in this population. From the polarized emission, we derived detailed magnetic field patterns throughout the filaments that we used to estimate field strengths for four out of the six clumps. The average field strength estimates were found to lie between 500 μG to 1.8 mG. Additionally, we detected and modeled infalling motions toward MM2 and MM3 from single-dish $HCO^+(J = 4 \rightarrow 3)$ and $HCN(J = 4 \rightarrow 3)$ data, resulting in mass infall rates of $\dot{M}_{\rm MM2} = 1.2 \times 10^{-2}$ $M_{\odot}\,{\rm yr}^{-1}$ and $\dot{M}_{\rm MM3} = 6.3 \times 10^{-3}\,M_{\odot}\,{\rm yr}^{-1}$. Using our estimations, we evaluated the dynamical equilibrium of our cores by computing the total virial parameter $\alpha_{\rm total}$. For the cores with reliable field estimates, we found that 71% appear to be gravitationally bound while the remaining 29% are not. We conclude that these unbound cores, which are also less massive, are still accreting and have not yet reached a critical mass. This also implies different evolutionary timescales, which essentially suggests that star formation in high-mass filaments is not uniform.

Key words: ISM: clouds – ISM: kinematics and dynamics – ISM: magnetic fields – stars: formation

1. Introduction

The formation of high-mass stars still eludes a comprehensive and detailed theoretical model. As these high-mass stars are born inside giant complexes of molecular gas and dust (GMCs), which are mostly more than 1 kpc away from the Sun, resolving them into detail images has been a historical problem. This has radically changed with the rise of a new generation of powerful millimeter and submillimeter facilities, such as ALMA, which have provided us with unprecedented data about the GMCs and the high-mass star formation process. Given the large amount of gas and dust needed to assemble GMCs, the high-mass star formation process is much more dynamic and complex than what we see in the nearby low-mass star-forming regions.

High-mass stars are usually encountered in dense clusters composed of up to many million stars (Weidner et al. 2010). The formation of such clusters requires large reservoirs of gas, which are likely the result of the fragmentation of massive clumps of weakly ionized and magnetized gas and dust inside GMCs. Thus, the formation of high-mass stars cannot be decoupled from the study of associations, where the cluster environment plays a significant role.

There are currently two competing theoretical views for the high-mass star formation process: (1) The core accretion model, which starts from a fragmented clump of self-gravitating, centrally condensed core of gas and dust that will collapse into one or more stars. The final mass is determined by the accretion of material from their surroundings. This scenario predicts that high-mass stars will form disks around them as accretion proceeds. (2) The competitive accretion model assumes instead that the formation process is more chaotic and controlled by turbulence. In this model there is no gravitationally bound prestellar phase, and the final mass is determined by competitive accretion from the swarm of cores produced by turbulence. If the density is sufficiently high, star collisions might also contribute to the final mass of the star. For a detailed review, see Tan et al. (2014).

[16] NAOJ Fellow.

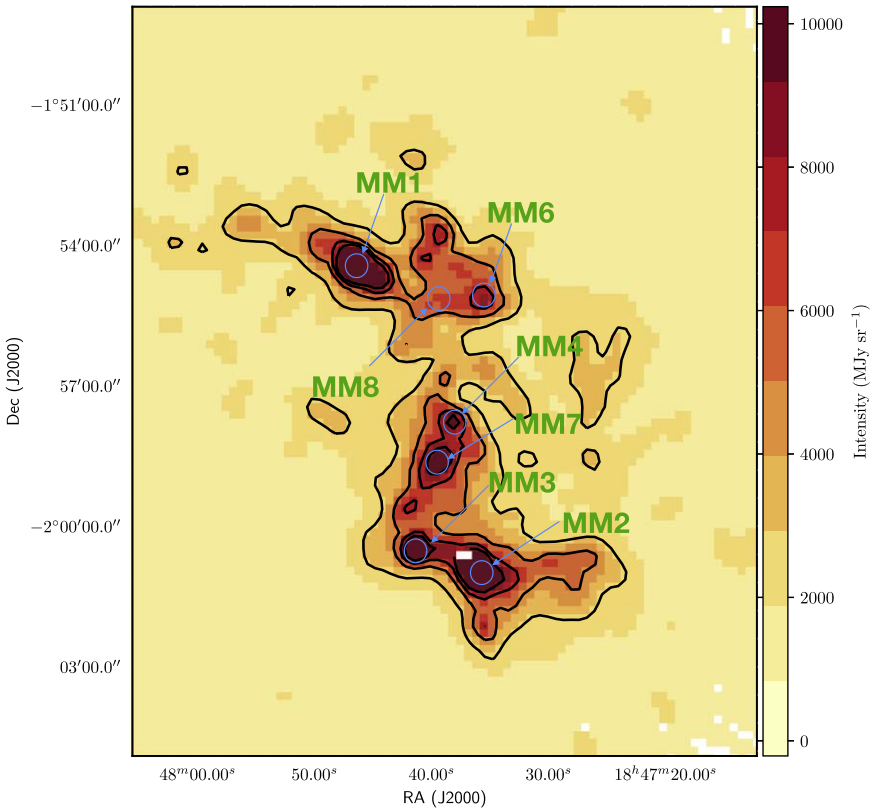

Figure 1. Overview of the W43-Main molecular complex with the location of its most massive clumps. Here we show Shark 350 μm data from W43-Main in black contours superposed on the color scale (data taken from Figure 1(b) from Motte et al. 2003). With blue circles we show the approximate locations of the clumps observed with ALMA and their respective names. The circles do not represent size and are used for indicative purposes only.

The large molecular complex W43-Main is located within the W43 region at 5.5 kpc from the Sun (Motte et al. 2003; Zhang et al. 2014). The cloud is near $l = 31°$, $b = 0°$ and at an interface with an extended H II region powered by a cluster of OB type and Wolf–Rayet stars (Cesaroni et al. 1988; Liszt 1995; Mooney et al. 1995; Blum et al. 1999). Although the exact number is uncertain, it is believed that the W43 cluster harbors about 50 OB stars with a total luminosity of about $3.5 \times 10^6\,L_\odot$. Some of the stars in the cluster are suggested to be WN7 class W-R stars, where W43-1 has an estimated bolometric magnitude of $M_{\rm bol} \sim 11.5$ mag compared with $M_{\rm bol} \sim 11.7$ mag for the Pistol star in the Galactic center Quintuplet cluster (Blum et al. 1999; Rahman et al. 2013). These stars belong to the most massive end of the distribution, and their influence on the surrounding gas should therefore not be underestimated.

The W43-Main complex (see Figure 1 for an overview) has been well studied in continuum from 1.3 mm to 70 μm (Motte et al. 2003; Bally et al. 2010) as well with large surveys of CO (Carlhoff et al. 2013), HCO^+(3-2) (Motte et al. 2003), and HCO^+(1-0) and H42α (Nguyen-Luong et al. 2017). These studies identified a large sample of clumps in the W43-Main molecular complex. The W43-MM1 clump has already been revealed as the most massive clump with an estimated mass of about 3000 $M_\odot$ and a deconvolved size of ∼0.1 pc (Cortes & Crutcher 2006; Louvet et al. 2014; Sridharan et al. 2014). The clump appears to be a fully fragmented and magnetized filament, with large-scale infalling motions (Cortes et al. 2010), and with a massive condensation dominating most of the flux from the clump (core *A* in Sridharan et al. 2014; Cortes et al. 2016). Recently, Motte et al. (2018) presented detailed high-resolution (0.01 pc scales) ALMA data of W43-MM1. In their data, they detected 131 cores with masses ranging from 1 to 102 $M_\odot$, where core *A* was resolved into a binary system of massive cores. The derived core mass function (CMF) has a slope that is consistently shallower than the currently assumed initial mass function (IMF; Bastian et al. 2010). This challenges the origin of the IMF because it cannot be simply inherited from the shape of the CMF.

Given the magnetized nature of these structures, it is of paramount importance to map the magnetic field. Initial studies of the magnetic field using polarized dust emission with single-dish telescopes focused on the large scales, while later individual cores were mapped with interferometers. From these studies, there is mounting evidence of the dynamical importance of the magnetic field as indicated by the "hour-glass" morphologies seen at different length scales (Schleuning 1998; Girart et al. 2009; Qiu et al. 2014). For a detailed review see Hull & Zhang (2019). In W43-Main, our group started by mapping the brightest clump in the millimeter, W43-MM1 (Cortes & Crutcher 2006; Sridharan et al. 2014), where Cortes et al. (2016; hereafter Paper I) presented the first ALMA observations with high spatial resolution of polarized dust emission. From this study, we obtained magnetic field strengths on the order milliGauss for densities of a few $10^7\,{\rm cm}^{-3}$. The field morphology appears to be ordered over most of the filament, which is consistent with a strong field. From estimations of the strength of the field, we determined that the magnetic field appears to be weaker than gravity, and thus the cores in W43-MM1 would be collapsing, unless additional

sources of energy are considered. Estimations of the mass-to-magnetic flux ratio suggest that the cores are mostly supercritical and the field lines are being dragged by gravity around the dominant binary system.

To proceed with the investigation about star formation in W43-Main, we have selected the following six most massive clumps from the survey reported by Motte et al. (2003). Thus, in this paper we report the ALMA observations of polarized dust emission toward the W43-MM2, MM3, MM4, MM6, MM7, and MM8 clumps obtained in band 6 at 1.3 mm. Here, Section 2 reports the observations and calibration, Section 3 the continuum emission results, source extraction, magnetic field results, line emission results, and infall modeling for W43-MM2 and W43-MM3, Section 4 is the discussion, and Section 5 is the summary and discussion.

2. Observations

2.1. Alma Observations

The data presented here correspond to ALMA observations at 1.3 mm (band 6), project 2013.1.00725.S, obtained on 2015 May 30 over the seven brightest clumps from W43-Main (where W43-MM1 results were presented in Paper I). As part of a multi-field observation, the phase center coordinates for each clump were taken from Table 1 in Motte et al. (2003). An array of 35 antennas was used, reaching an angular resolution of $\sim 0\farcs5$ ($\sim$0.01 pc scales at a distance of 5.5 kpc). The spectral configuration was set to continuum mode (or TDM), with 64 channels per spectral window, giving a spectral resolution of 31.25 MHz in full polarization mode (where *XX*, *YY*, *YX*, and *XY* are the visibilities produced by the ALMA baseline correlator). Each spectral window was centered at the standard ALMA band 6 polarization frequencies (224, 226, 240, and 242 GHz). At the reference frequency, $\nu_{\rm ref} = 233$ GHz, the 12-meter antenna primary beam is $\sim 25''$. Two successful executions were made using the session scheme, which is described in Remijan et al. (2018). Calibration and imaging was made using the Common Astronomical Software Applications (CASA; version 4.7 McMullin et al. 2007). In total, we obtained about 12 minutes per field (clump), which gave an average rms for Stokes *I* of $\langle \sigma_{\rm I} \rangle \sim 200\ \mu$Jy beam^{-1} while the average rms for the polarized intensity is $\langle \sigma_{\rm poli} \rangle \sim 54\ \mu$Jy beam^{-1}. This is equivalent to a mass sensitivity of 0.08 $M_\odot$ under the assumptions made in Section 3.1.

2.2. Calibration and Imaging in Full Polarization Mode

The ALMA antennas are equipped with linearly polarized receivers. After reception of the incoming radiation, the wave is divided into two orthogonal components (*X* and *Y*) by a wave-splitting device (Remijan et al. 2018). This operation is not perfect and there is always a residual, or projection, from one polarization onto the other, which is known as the instrumental polarization, or D-terms (Hamakerr & Bregman 1996). Given that the antenna frame uses azimuth and elevation coordinates, the frame of the sky rotates with respect to the antenna, introducing an angular dependence that is parameterized by the parallactic angle. In addition to the D-terms, the *X* and *Y* polarizations have sligthly different analog signal paths inside the receivers before digitization, which introduces a relative delay between the two polarizations. Also, the interferometric calibration scheme for amplitude and phase requires the use of a reference. This reference breaks the degeneracy intrinsic to the array, and thus we do not measure absolute phase values but relative values with respect to the reference (where phases are set to zero in both polarizations). By doing this, we introduce an additional phase bandpass between the *XY* and *YX* cross correlations.

To calibrate all these quantities, an ALMA polarization observation samples a strong, unresolved, polarized source over a certain range of parallactic angle. The polarization calibrator is sampled for 5 minutes approximately every 35 minutes. For our observations, we obtained a coverage of about 100° of parallactic angle for J1924-292, which was selected as polarization calibrator. Using this source, we derived solutions for the cross-polarization delay, the *XY*-phase, and the D-terms. These solutions were applied to all the clumps in our data, along with J1751+0939 to calibrate the bandpass, J1851+0035 to calibrate the phase, and Titan to calibrate the flux. After applying the calibration tables, we imaged the data using the *clean* CASA task with the Briggs weighting scheme, robust number 0.5, for sidelobe robustness and the clarkstokes deconvolution algorithm to produce the Stokes images. The final images were produced after three phase-only self-calibration iterations using a final solution interval of 90 seconds.

2.3. ASTE Observations

The second and third most massive clumps from W43-Main (W43-MM2 and W43-MM3) were observed during 2010 July using the Atacama Sub-millimeter Telescope Experiment (ASTE) of the National Astronomical Observatory of Japan (NAOJ; Kohno 2005). The telescope is located at an altitude of 4900 m at Pampa la bola in the Chilean Andes plateau reserve for astronomical research. The ASTE telescope is a dish with a diameter of 10 m, equipped with a wide range of instruments, including a 345 GHz double side-band SIS-mixer receiver. We simultaneously observed $HCO^+(J = 4 \rightarrow 3)$ and $HCN(J = 4 \rightarrow 3)$ with a beam size of $\sim 22''$ and a velocity resolution of 0.1 km s^{-1} by setting the XF-type digital spectro-correlator to a bandwidth of 128 MHz. The pointing accuracy was about $2''$ with VY_CMA used as the pointing source. The observations were made by performing on-the-fly mapping (OTF) with a grid spacing of $10''$ and operating the telescope remotely from the ASTE base in San Pedro de Atacama under good weather conditions (precipitable water vapor, or PWV, < 1 mm). Our reference positions for MM2 and MM3 were taken from Table 1 in Motte et al. (2003). All temperatures are presented as $T_{\rm mb} = T_{\rm A}^*/\eta_{\rm mb}$, where $\eta_{\rm mb} = 0.71 \pm 0.07$. Initial data reduction and calibration was performed using the NEWSTAR package (Ikeda et al. 2001). The calibrated data were later exported to be plotted using matplotlib (Hunter 2007).

3. Results

3.1. Dust Continuum Emission

Continuum emission results from the W43-MM2, MM3, MM4, MM6, MM7, and MM8 clumps are presented in this section and shown in Figures 2, 3, 5, and 6–8. The ALMA data uncovered filamentary structure inside all of these clumps. Additionally, we resolved them into two populations, where the MM6, MM7, and MM8 clumps (population 1) present major fragmentation when compared to the MM2, MM3, and MM4 clumps (population 2). This later population also appears to have a dominant region in the emission, which we later

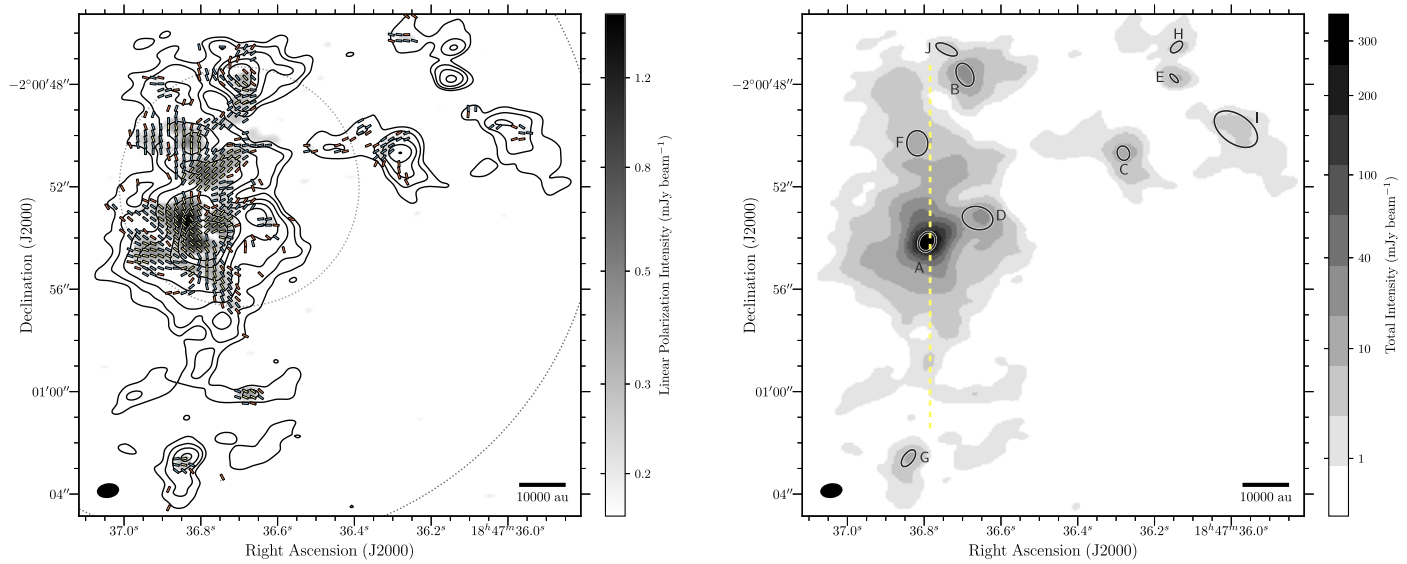

Figure 2. Stokes *I* emission (*right*) and magnetic field map (*left*) from the W43-MM2 clump as resolved by ALMA. The magnetic field map is composed of a total intensity image (Stokes *I*) in contours of 4, 8, 16, 32, 64, 128, and 256 × σ_I, where $\sigma_I = 245\ \mu$Jy beam^{-1}, the polarized intensity image in gray scale, with $\sigma_{\rm poli} = 58\ \mu$Jy beam^{-1}, and the magnetic field map in pseudo-vectors of 2.5 (red), 3 (blue), and >5$\sigma_{\rm poli}$ (yellow), which was constructed by rotating the polarization position angle (EVPA) by 90°. We plot two circles as black dotted lines to indicate the 1/3 FWHM and FWHM primary beam (field of view). The 1/3 FWHM covers the area where the ALMA polarization accuracy, or minimum detectable polarization, is 0.1%. The total intensity Stokes *I* emission map is shown to the right in a gray scale of mJy beam^{-1} as indicated by the color bar. Overlaid are the cores we extracted, and they are indicated as ellipses in black. These ellipses represent the deconvolved size obtained from the Gaussian fits. The yellow dashed line corresponds to the main axis of the filament. In both maps, the bar at the bottom right corner gives the spatial scale in au.

identified as a massive core. It is also relevant to note here that there is a fundamental difference in the strength and distribution of the polarized emission we detected between the two populations. In population 1, the polarized intensity is weaker and compact, while in population 2, the polarized emission is strong and widely distributed over significant parts of the clumps.

As in Paper I, we used the *getsources* algorithm (Men'shchikov et al. 2012) to extract core candidates from the continuum emission. The extracted core position and size was used as a seed for a 2D Gaussian fitting by means of the CASA task imfit used over the primary beam corrected maps. From this, we obtained accurate fluxes, positions, and sizes. However, only cores where the Gaussian fitting converged were considered here, although using this additional step (the 2D Gaussian fitting) may overestimate the core flux because the deconvolved Gaussian area may be more extended than the original size obtained from getsources. Our method provides an increased degree of confidence in the likelihood of the extracted cores given the convergence criteria required to fit the Gaussian. We chose to do this because we did not meet the expected sensitivity and the resulting beam shape was more elongated than expected due the to the low elevation reached by the end of the session. Later, we calculated the core parameters by first computing the column density and the mass as

$$N_{\rm H_2} = \frac{S_\nu}{B_\nu(T)\Omega\kappa_\nu\ \mu m_{\rm H}} \quad (1)$$

$$M = \Omega\ \mu m_{\rm H} N_{\rm H_2} d^2, \quad (2)$$

where S_ν is the total flux obtained from the Gaussian fitting, $B_\nu(T)$ is the Planck function, and T is the dust temperature. The source size is given by the solid angle Ω, which we also obtained from the Gaussian fitting, $\kappa_\nu = 0.01\ {\rm cm^2\ gr^{-1}}$ is the emissivity of the dust grains at 230 GHz, which includes a gas-to-dust ratio of 100 (Ossenkopf & Henning 1994). The $\mu = 2.33$ is the mean molecular weight and $m_{\rm H}$ is the mass of hydrogen in grams. Finally, d corresponds to the distance to W43-Main, estimated to be 5.5 kpc (Zhang et al. 2014). The column density calculation assumes that the dust emission is optically thin. Although this assumption might break down to the most dense cores, it is still a reasonable approximation on average for most of them. The temperature range used in the mass calculation was taken from the spectral energy density (SED) fitting by Motte et al. (2003) and Bally et al. (2010), performed over MM2, MM3, and MM4, which are the most massive clumps. For MM6, MM7, and MM8, we assumed $T = 25$ K, which is the mean value of the temperatures determined by the SED fitting and representative of the temperature of the ambient molecular gas.

3.1.1. W43-MM2 Continuum

The W43-MM2 (hereafter MM2) clump is the second largest clump from the Motte et al. (2003) continuum survey. The most recent mass estimation places MM2 in the (3.5–5.3) × $10^3\ M_\odot$, where the estimate was made by Bally et al. (2010), assuming an overall dust temperature of 23 K. In fact, this mass estimate means that MM2 is the most massive clump in W43-Main. The presence of OH and CH_3OH maser emission together with the lack of centimeter and 24 μm emission indicates that it is a high-mass star-forming clump in an early evolutionary stage. In addition, no molecular outflow has been detected so far. Figure 2 shows the ALMA 1 mm total intensity continuum map as well as the polarization map (see Section 3.2). The clump appears as a fragmented filament at length scales of 0.01 pc where the emission seems dominated by a single source, which seems to be the case for population 2 or the most massive clumps presented here. We label this

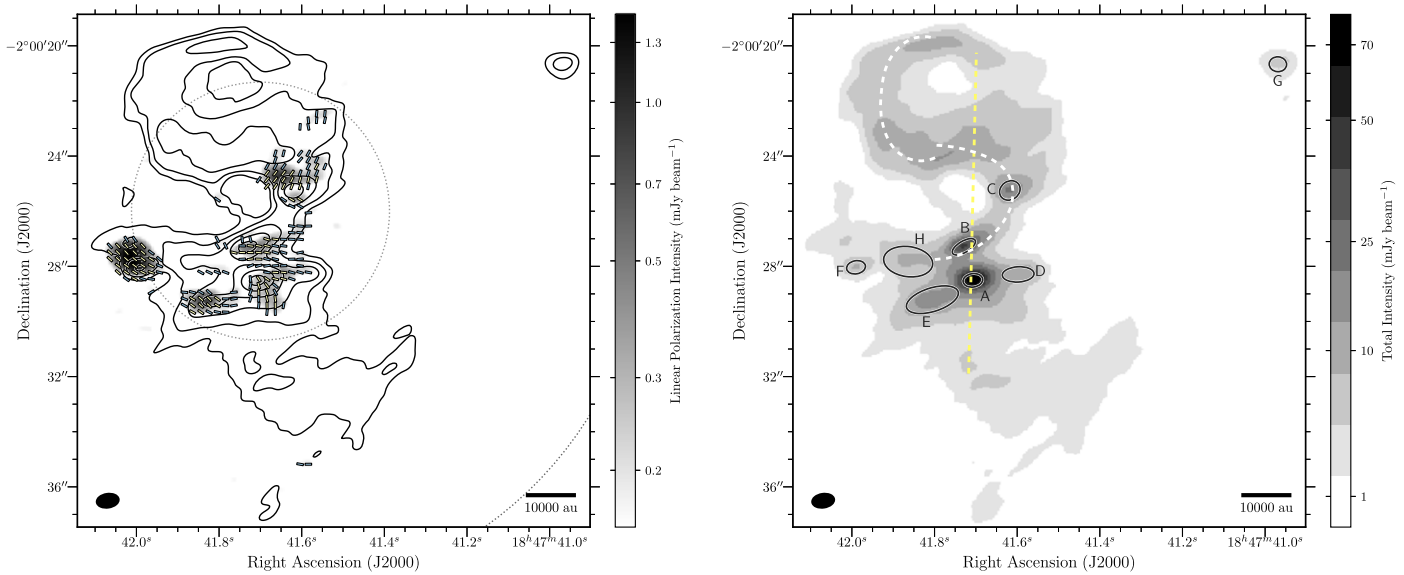

Figure 3. Stokes *I* and magnetic field maps for the W43-MM3 clump as shown by Figure 2. To the *left*, the Stokes *I* is represented in contours of 8, 16, 32, 64, 128, and 256 × $\sigma_{\rm I}$, where $\sigma_{\rm I} = 240$ μJy beam^{-1}, the polarized intensity image in gray scale, with $\sigma_{\rm poli} = 52$ μJy beam^{-1}, and the magnetic field map in pseudo-vectors of 2.5 (red), 3 (blue), and >5$\sigma_{\rm poli}$ (yellow). The total intensity Stokes *I* emission map is shown to the *right* in a gray scale of mJy beam^{-1} as indicated by the color bar. Overlaid are the sources we extracted as ellipses, in black, representing the deconvolved size obtained from the Gaussian fits. The yellow dashed line corresponds to the main axis of the filament, while the white dashed lines indicate the cavities, or shell, seen in the dust continuum map.

source core *A* to follow the nomenclature from paper I, with a total recovered flux of 880 mJy and an estimated mass of 426 $M_\odot$. This core has ∼63% of the total flux from all the detected cores in MM2. It also appears to be monolithic, with no obvious indication of further fragmentation, although higher resolution observations with ALMA will indicate if the core has substructure. We treat the mass estimate of 426 $M_\odot$ as an upper limit given that it is unlikely that MM2-*A* is as cold as 23 K. Sridharan et al. (2014) detected a high-temperature hot core in MM1-*A* that had a similar initial mass estimate. However, and given that we do not have spectral line data from MM2-*A* at sufficient resolution, we can only speculate about the evolutionary stage of the core. Table 3 presents the source extraction parameters for this clump. The mass estimate derived here assumes $T_{\rm d} = 23$ K for all the cores in the clump.

3.1.2. W43-MM3 Continuum

W43-MM3 (hereafter MM3) is located in the southern part of W43-Main and to the east of MM2, with an estimated total mass between 1.5 and 2.3 × 10^3 $M_\odot$ (Bally et al. 2010). The MM3 clump has been identified to contain the G30.720-0.083 radio continuum source showing emission from 0.6 to 21 cm, with a peak flux of 115 mJy at 6 cm, which is the brightest UC H II region in W43 (Bally et al. 2010). The MM3 is also seen as an infrared dark cloud (IRDC) in absorption at 70 μm and as bright clump at 160 μm, as shown by *Herschel* data (Bally et al. 2010). In the ALMA data (see Figure 3), the MM3 clump appears as a fragmented filament, with eight extracted cores, where core *A* is the dominant core with a total flux of 150 mJy at 1 mm and an estimated mass of 59.4 $M_\odot$. The MM3 filament shows a double cavity feature, or maybe a dust shell, to the north of core *A*, with an S-type morphology as seen from north to south (as indicated in Figure 3). Furthermore, the cavity to the north is not associated with any millimeter-detected source.

To ascertain the nature of this shell, we obtained *SPITZER* IRAC archival images toward MM3. Figure 4 shows the MM3 ALMA contours superposed on the IRAC map, where two sources, or stars, appear to coincide with the shell. The stars are indicated with red and green circles. Moreover, the G30.720-0.083 UC H II region (α, δ = 18:47:41.808, −02:00:23.76) is also located within the shell and close to one of the IRAC sources (Zoonematkermani et al. 1990). The resolution of the Very Large Array (VLA) data used to detect G30.720-0.083 is about 5″, which is about the size of the shell. Despite the uncertainty introduced by the coarse VLA resolution, it is plausible that the UC H II region coincides with one of the IRAC sources, and thus the UC H II region might explain the origin of the shell. We should note that the 8σ to 16σ contours around the shell are closer toghether than the more significant contours, which may indicate spherical symmetry. Alternatively, morphologies like this have been observed as the result of outflow emission. Outflows can carve cavities around the envelope of a star, as seen in a number of regions. Hull et al. (2016) and Maury et al. (2018) presented a clear example in Serpens SMM1 and B335. In the SMM1 core a high-velocity jet of ionized gas and a highly collimated molecular outflow are carving a cavity around the young Class 0 protostellar source powering the jet. In B335 the east–west outflow has carved a cavity whose walls are clearly visible in their ALMA data. This scenario might explain the southernmost cavity because cores *B* and *C* are geometrically close to power the outflows. However, we have no data to search for outflow emission from the *B* and *C* MM3 cores. Furthermore, the northernmost cavity is difficult to explain in this way because we lack an explicit core detection nearby. For this clump, the core mass distribution extends from 6.6 to 59.4 $M_\odot$, where we used $T_{\rm d} = 27$ K uniformly.

3.1.3. W43-MM4 Continuum

The W43-MM4 (hereafter MM4) is also associated with a radio continuum source. Balser et al. (2001) suggested the presence of an UC H II region at the center of MM4, while

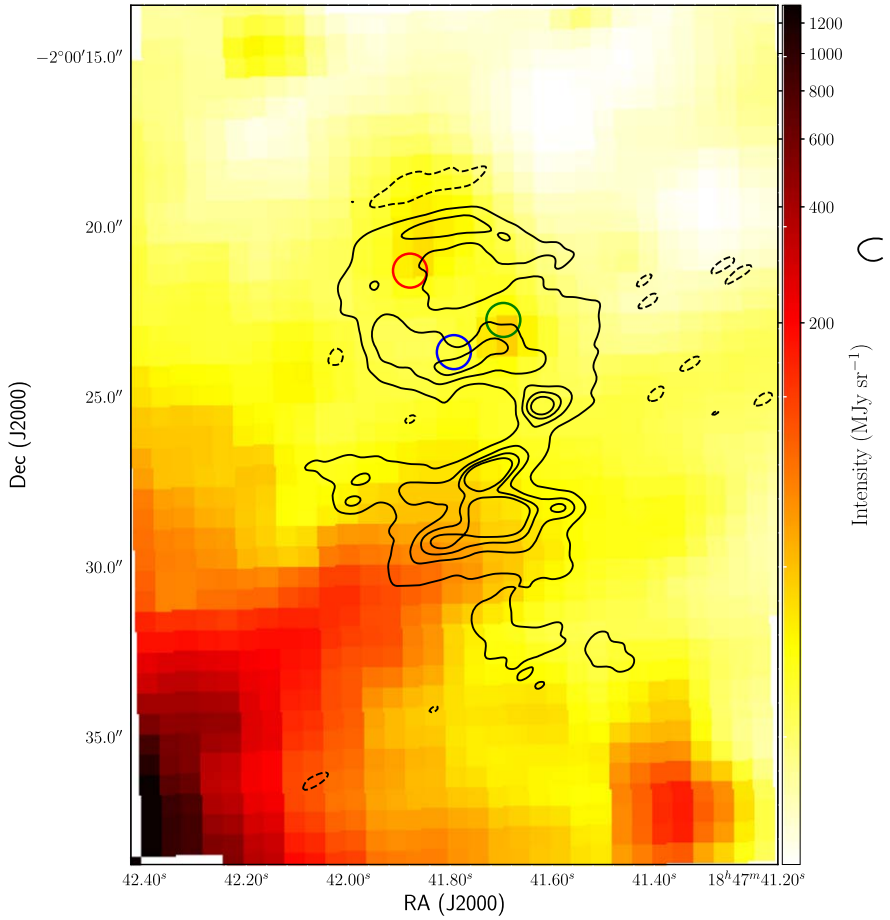

Figure 4. Dust emission in contours from the MM3 clump. Superposed in color is an archival IRAC 3.6 μm *SPITZER* image from the same region. To the southeast a bright source is shown, which appears to be a foreground star. To the north lie two stars that seem to coincide with the dust shell seen in MM3; they are indicated by red and green circles. The estimated surface brightness is 31 $\pm$ 6 MJy sr^{-1} for the red star and 27 $\pm$ 5 MJy sr^{-1} for the green star. Using a blue circle, we also indicate the position of G30.720-0.083 from the VLA data.

Zoonematkermani et al. (1990) found coincidence with strong free–free emission ($\sim$300 mJy), typical from UC H II regions. However, the resolution of both detections is coarse ($\sim$9″ and 5″), which makes it difficult to correlate with our higher resolution ALMA data. This clump is also one of the closest in our sample to the W-R/OB cluster powering up W43, with a projected distance of about 2 pc. This distance is close enough to consider the clump inside the shock and the ionization fronts from the W43 giant H II region.[17] However, SiO(2–1) maps of W43-Main presented by Nguyen-Lu'o'ng et al. (2013) show insignificant emission toward MM4. Although the authors attribute the SiO emission to a low-velocity shock produced by colliding flows, we would have expected an enhancement in the SiO emission and the development of photoionized regions (PDRs) from MM4 given its proximity to the W43 H II region.

Bally et al. (2010) estimated an MM4 clump mass between 0.9 to 1.3 $\times$ 10^3 $M_\odot$ assuming an overall $T_{\rm d}$ = 28 K. This temperature is consistent with estimations reported by Nguyen-Lu'o'ng et al. (2013) based on the UV radiation field illuminating this clump. Figure 5 shows the ALMA map of MM4, where the emission appears distributed around the main peak with a tail toward the southeast. Source *A* dominates the emission with a flux of 160 mJy, although we did not resolve it, as shown in Figure 5. Another seven sources are also detected mainly around core *A*, the dominant source in MM4 and a likely candidate for a UC H II region. Three additional cores are detected toward the southwest, *C*, *G*, and *D*. They appear to be connected to the main filament, although it is interesting to see that no sources were detected within the bridge that joins the tail with the main filament. The core mass estimates for MM4 are listed in Table 3.

3.1.4. W43-MM6, MM7, and MM8 Continuum

The initial mass estimate from Motte et al. (2003) places these clumps in the <1000 $M_\odot$ regime, where the estimates are $\sim$500 $M_\odot$ for MM6, $\sim$870 $M_\odot$ for MM7, and $\sim$390 $M_\odot$ for MM8. Current data from W43-Main suggest no radio continuum and/or infrared/far-infrared detections sources associated with these clumps. Thus, they seem to be in an early stage of evolution. As these clumps have not been extensively studied, we lack detailed SEDs for them. Therefore, we assumed a dust temperature of $T_{\rm dust}$ = 25 K for all three of them because this seems a representative value considering their fluxes and the temperatures assumed for the other clumps. The source parameters for the cores we extracted from these clumps are listed in Table 3.

The MM6 clump shows a clear filamentary structure with 10 cores detected along the major axis and 2 cores to the east.

[17] A quick calculation for the Strömgren radius for the W43 H II region gives R_s = 4.3 pc when we assume that the number of Lyman continuum photons per star is 6.0 $\times$ 10^{49} (with $\sim$100 stars, or 10^{51} Lyman continuum photons per second in total) and an electron density of n_e = 10^3 cm^{-3} (Blum et al. 1999).

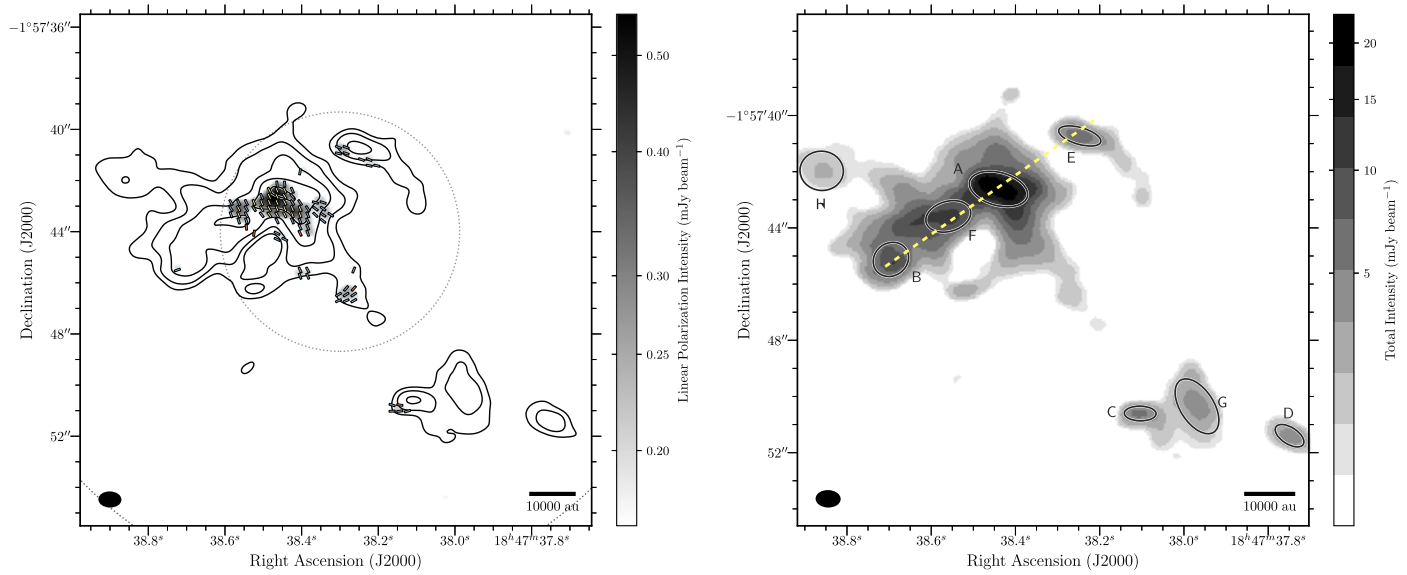

Figure 5. Stokes *I* and magnetic field maps for the W43-MM4 clump as shown by Figure 2. To the *left*, the Stokes *I* is represented in contours of 4, 8, 16, 32, 64, and 128 × $\sigma_{\rm I}$, where $\sigma_{\rm I} = 324 \mu$Jy beam^{-1}, the polarized intensity image in gray scale, with $\sigma_{\rm poli} = 56$ μJy beam^{-1}, and the magnetic field map in pseudo-vectors of 2.5 (red), 3 (blue), and >5$\sigma_{\rm poli}$ (yellow). The total intensity Stokes *I* emission map is shown to the *right* in a gray scale of mJy beam^{-1} as indicated by the color bar. Overlaid are the sources we extracted as ellipses in black, representing the deconvolved size obtained from the Gaussian fits.

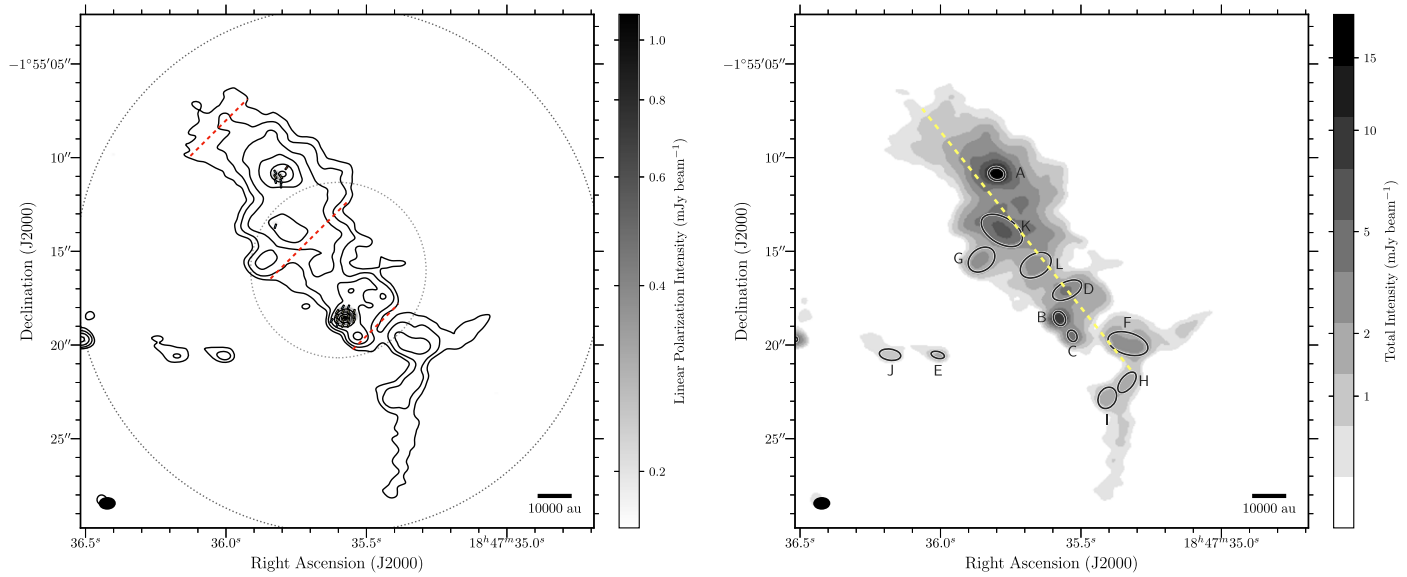

Figure 6. Stokes *I* and magnetic field maps for the W43-MM6 clump as shown by Figure 2. To the *left*, the Stokes *I* is represented in contours of 4, 8, 16, 32, 64, and 128 × $\sigma_{\rm I}$, where $\sigma_{\rm I} = 131$ μJy beam^{-1}, the polarized intensity image in gray scale, with $\sigma_{\rm poli} = 54$ μJy beam^{-1}, and the magnetic field map in pseudo-vectors of 2.5 (red), 3 (blue), and >5$\sigma_{\rm poli}$ (yellow). The dashed red lines show the cuts we used to estimate the filament width. The total intensity Stokes *I* emission map is shown to the *right* in a gray scale of mJy beam^{-1} as indicated by the color bar. Overlaid are the sources we extracted as ellipses in black, representing the deconvolved size obtained from the Gaussian fits. The yellow dashed line indicates the main axis of the filament.

Figure 6 shows the MM6 ALMA map and the detected cores. From a total of 12 detected cores, the brightest, labeled *A*, has an integrated flux density of 52 mJy and and a deconvolved size of 0.02 pc. From Table 3, we see that core *K* has a higher integrated flux than *A*. However, this is because the deconvolved size from the Gaussian fit is larger and so consequently is its integrated flux. Now and by looking at the peak flux, core *A* is clearly the dominant source in the clump, with 20.5 mJy beam^{-1} compared to 6.5 mJy beam^{-1} from *K*. The core estimated masses are within the <25 $M_\odot$ regime for MM6, and and their mass distribution appears to be uniform even when we consider the most massive cores *A* and *B*. This is a departure from what is seen in the other W43-Main clumps, where the brightest cores in MM1 (see Paper I and Motte et al. 2018), MM2, MM3, and MM4 significantly dominate the core mass distribution of their respective clumps. Given the clear filamentary morphology of MM6, we can directly calculate its width,[18] which on average is closer to 4.″3 or 0.12 pc assuming 5.5 kpc as the distance to the Sun. Now, the maximum recoverable angular scale for our data is about 5.″12 or 0.14 pc. Thus, the filament width is within the length scales that ALMA

[18] The filament width was calculated as an average of three measurements, top, middle, and bottom (shown as dashed red lines on top of the contour maps for each clump), which was made following the main axis of the filament. The distance was computed from a line that connects the lowest contour from their respective map while crossing the main axis highest contour.

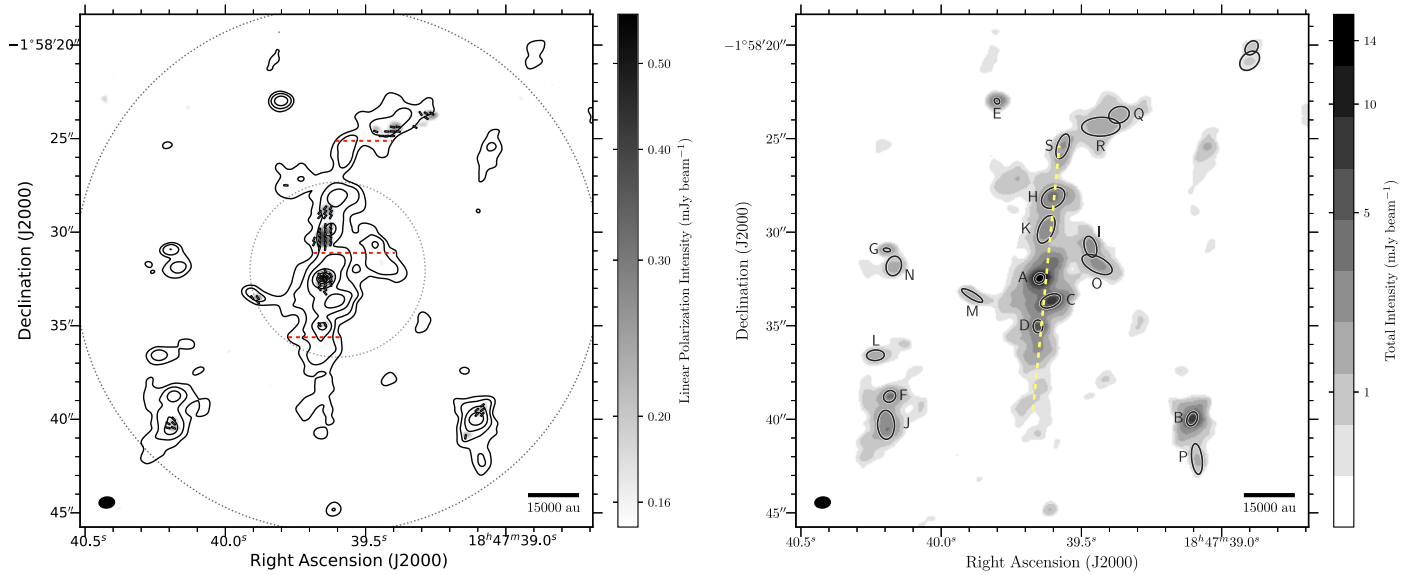

Figure 7. Stokes *I* and magnetic field maps for the W43_MM7 clump as shown by Figure 2. To the *left*, the Stokes *I* is represented in contours of 4, 8, 16, 32, 64, and 128 × $\sigma_{\rm I}$, where $\sigma_{\rm I} = 150$ μJy beam^{-1}, the polarized intensity image in gray scale, with $\sigma_{\rm poli} = 50$ μJy beam^{-1}, and the magnetic field map in pseudo-vectors of 2.5 (red), 3 (blue), and >5$\sigma_{\rm poli}$ (yellow). The dashed red lines show the cuts we used to estimate the filament width. The total intensity Stokes *I* emission map is shown to the *right* in a gray scale of mJy beam^{-1} as indicated by the color bar. Overlaid are the sources we extracted as ellipses in black, representing the deconvolved size obtained from the Gaussian fits. The yellow dashed line indicates the main axis of the filament.

is sensitive to, and it therefore does not seem to be a cutoff given by the array configuration. Although such filament widths were initially seen toward low-mass star-forming regions (Arzoumanian et al. 2011), data obtained from single-dish mapping suggest that a similar filament length scale might also be present in high-mass star-forming regions (André et al. 2016).

In the MM7 clump, shown in Figure 7, we detected 11 cores along the central filament, with 9 additional cores to the east and west. Cores *A* and *B* dominate the emission, but with a peak flux distribution similar to what we see in MM6 and flatter than what is seen in the other most massive clumps. In total, we extracted 20 cores from MM7, which is about a factor of two more than what we have obtained in the most massive clump from our sample (MM2). This implies a higher fragmentation level, but with a more uniform mass distribution (from 1.7 to 11.8 $M_\odot$). The estimated mass for core *A*, 11.7 $M_\odot$, is about a factor of six lower than the MM3 and MM4 dominant cores, and a factor 40 lower than the MM2 core *A*. However, this mass seems sufficient to form a high-mass star, especially if accretion is still ongoing. The MM7 clump also shows a clear filamentary structure with an average width of about 3.″5 or 0.09 pc.

The MM8 clump has the lowest mass in our sample. Here, we detected a total of 18 cores with a peak flux distribution similar to that in MM7 and MM6. Three of the detected cores dominate the peak flux: cores *A*, *B*, and *D*. This is in line with what is seen in the MM6 and MM7 clumps (population 1). In fact, in MM8 we see an increase in the number of low-mass cores, where some of them have a mass lower than 1 $M_\odot$. We recall that these sources are all significant detections with fluxes that are a least 10σ higher than the noise. The ALMA map for MM8 with the identified cores is shown in Figure 8. The MM8 clump also shows a filamentary structure, but in this case, the peak of the clump emission was offset from the phase center by ∼20″. The filament width is on average about 2.″4 or 0.06 pc, which is similar to MM7.

In general, we find that all the clumps in the W43-Main molecular complex show a filamentary structure. Here, we define a filament as emission from the clump that shows a geometrically elongated morphology with a preferred direction. Additionally, we found that three of these clumps (MM2, MM3, and MM4) have one core that dominates the flux distributions and therefore the mass. The other three clumps (MM6, MM7, and MM8) have a flatter mass distribution with two to three cores dominating the emission. We also find in most clumps single and isolated cores that do not seem to be directly associated with the main filament (e.g., cores *G* in MM3 and *A* in MM8). Although fragmentation in these filaments is evident along the major axis, additional fragmentation is seen, sometimes in the orthogonal axis projection (such as MM4), as well as in filaments parallel to the main axis (e.g., MM7). In these cases, more than one core is detected. As we show below, this difference is also correlated with a difference in the amount of polarized emission detected from these filaments. The filaments that are dominated by a massive core are highly polarized, but the filaments with a flatter core-mass distribution are virtually unpolarized.

3.2. The Magnetic Field Strength from Dust Continuum Emission

We derived the magnetic field morphology onto the plane of the sky from the polarized emission assuming grain alignment with respect to the magnetic field for all clumps in our sample. We also estimated the magnetic field strength onto the plane of the sky, or $B_{\rm pos}$, using the Davis–Chandrasekhar–Fermi (DCF) method (Davis 1951; Chandrasekhar & Fermi 1953) and its variants (see Appendix A), as previously done in Paper I, over selected regions for each clump (see Figure 9). To do this, we used a number of assumptions, most notably that the velocity dispersion can be extrapolated from large scales by assuming a Kolmogorov-like power spectrum and the dispersion in the polarization position angle (also called the electric vector position angle, or EVPA) is due to perturbations from the

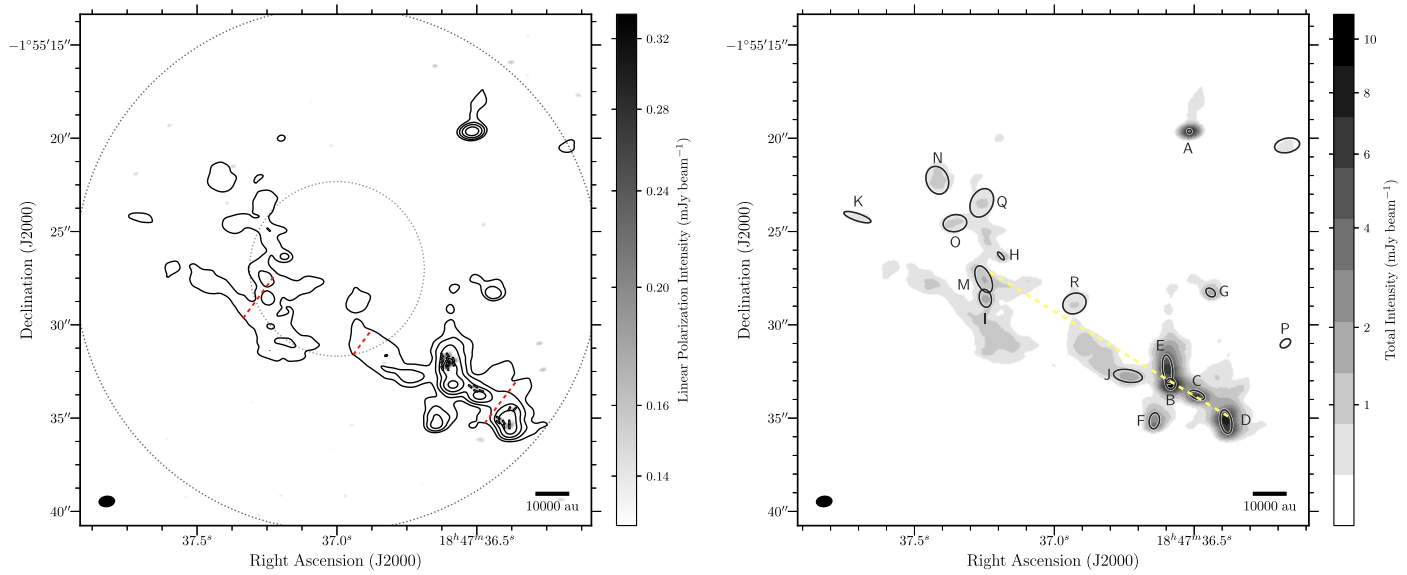

Figure 8. Stokes *I* and magnetic field maps for the W43-MM8 clump as shown by Figure 2. To the *left*, the Stokes *I* is represented in contours of 4, 8, 16, 32, 64, and 128 × $\sigma_{\rm I}$, where $\sigma_{\rm I} = 136$ μJy beam^{-1}, the polarized intensity image in gray scale, with $\sigma_{\rm poli} = 51$ μJy beam^{-1}, and the magnetic field map in pseudo-vectors of 2.5 (red), 3 (blue), and >5$\sigma_{\rm poli}$ (yellow). The dashed red lines show the cuts used to estimate the filament width. The total intensity Stokes *I* emission map is shown to the *right* in a gray scale of mJy beam^{-1} as indicated by the color bar. Overlaid are the sources we extracted as ellipses in black, representing the deconvolved size obtained from the Gaussian fits. The yellow dashed line indicates the main axis of the filament.

nonthermal motions of the gas. The details are discussed in Appendix A.

3.2.1. The W43-MM2 Field

The magnetic field morphology onto the plane of sky for the MM2 clump is shown in Figure 2. The polarized emission covers most of the Stokes *I* map at the 3σ level from north to south. The inferred magnetic field pattern is quite complex, showing areas on the map where the field appears to be coherent over significant portions of the filament. Over these areas, the EVPA dispersion is small, which is suggestive of strong fields. However, we have chosen larger regions to estimate the field strength in order to obtain a sufficient number of independent points and also to derive a representative value for the ambient magnetic field around the cores in a given region.

To the west of the main filament and over the MM2-*C* core, the field morphology suggests continuity with the field over the main filament, despite the gap seen in the total intensity. It is important to state that most of the polarized emission used to infer the field morphology and estimate its strength in this clump is within one-third of the primary beam of the ALMA 12 m antenna (inner dotted circle in Figure 2). Within this region, ALMA meets the specification of a minimum detectable amount of linear polarization of 0.1%. Outside this region, the specification is not guaranteed, but in band 6 the performance degradation is no worse than 0.6% at the 50% level of the FWHM with an error in the EVPA no larger than 2°. Thus, we are confident that the polarization morphology over MM2-*C* is representative of the magnetic field morphology.

To estimate the field strength throughout the MM2 clump, we have defined four regions based on the projected field apparent connectivity (see Figure 9). Region 1 was defined over sources *A* and *D* where the field shows a well-connected radial pattern. Toward core *A* in region 1, the field pattern is mostly radial, which is quite similar to the morphology seen toward MM1-A (Paper I). In that case, the interpretation was that gravity dominates and the field is being dragged toward the main core. We explore this possibility in the discussion section (see Section 4). To the north and over core *F*, we defined region 2, where the field is also continuous, well connected, and clearly distinct from the field morphology seen in region 1. Region 3 is defined over cores *B* and *J*, where the field pattern seems isolated and with a different morphology with respect to the field pattern seen in region 2. Region 4 is defined to the west over core *C*, where the field is isolated from the main filament. However, at the 2.5σ level, there seems to be continuity between the field in this region and the filament main field. Figure 9 shows the regions on top of the polarized intensity map. In all the four regions, the angular scale for the 3σ polarized emission is about 5″. We used this angular scale to calculate $\delta\phi$ and $\sigma_{\rm v}$. Table 4 shows the estimated $B_{\rm pos}$ for all the cores belonging to the chosen region.

We obtained field estimates from 0.1 to 3.2 mG throughout the clump (see Table 4). This range of field estimates is smaller to the values obtained toward W43-MM1, where the spread and morphology the polarized emission is similar. In MM1 the emission covered the entire filament, or ∼13″, which is about the extension of MM2 (∼14″) when we consider the entire polarized emission. The differences in the field estimates here compared to Paper I come from the values of ΔV where the Kolmorogov extrapolation give smaller line widths than the 3 km s^{-1} used there. Also, the regions used to calculate $\delta\phi$ in Paper I traced field patterns with lower dispersion values in the EVPA. In MM2, the situation is more complex as the field is clearly connected throughout the filament, which complicates the definition of these regions. It is important to point out that the DCF method assumes that the EVPA dispersion is the product of perturbations in the field lines by the nonthermal motions of the gas (a more detailed discussion can be found in A). However, in region 1, over the MM2-*A* core, the EVPA dispersion seems to be produced by infalling gas perturbations of the field lines rather than by turbulence (see Section 3.3 for our gas infalling results). One way to see this is by noting that

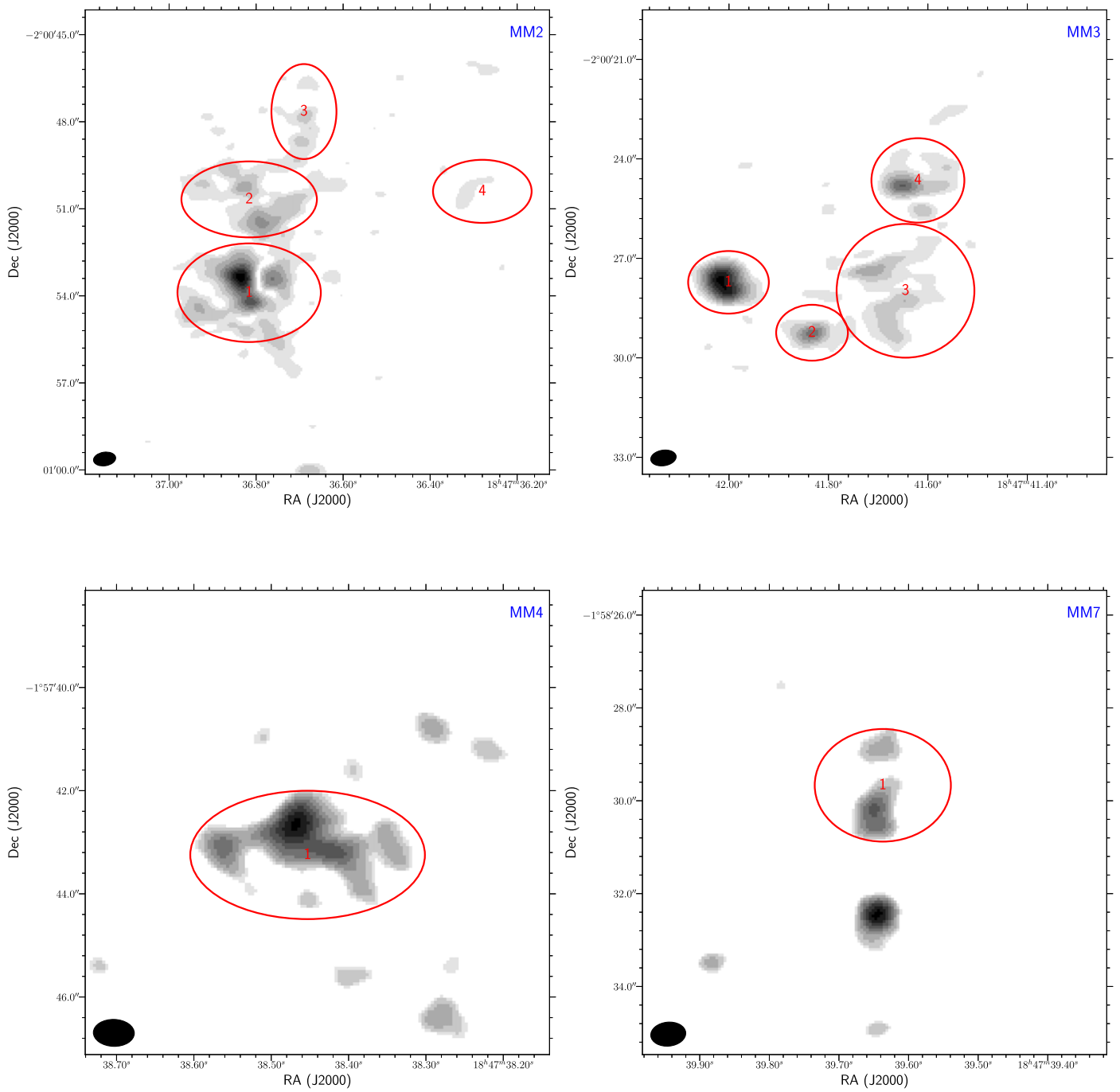

Figure 9. Polarized intensity maps for the MM2, MM3, MM4, and MM7 clumps. The polarized intensity emission is shown at the 3σ level for each clump. Superposed are the numbered regions as red ellipses, indicating the areas we defined to estimate $B_{\rm pos}$ in each clump. The clump name is indicated in blue in the top right corner.

the northeast and northwest pseudo-vectors toward the center of MM2-*A* seem to be almost orthogonal to each other. It is unlikely that turbulence induces this level of change in the field lines, and therefore it has come from gravity. Although in MM1-*A* we have a similar situation, the geometrical distribution of the polarized emission seemed to favor a bimodal distribution between two distinct subregions, but where one of them is more extended. As both regions have small EVPA dispersion, one dominated, which decreased the overall value of $\delta\phi$ (see Figure 2 in Paper I). This resulted in an increase in the estimated field strength when compared to MM2-*A*, although both regions have similar field morphologies. Therefore, this bias in the estimation of $\delta\phi$ likely yielded magnetic field strength estimates that are lower limits of the "true" magnetic field strength around the MM2-*A* and *D* cores. The same might be said from the estimation made toward MM1-*A* in Paper I.

Although the field lines around the main core (region 1) have a clear radial pattern, the field to the north is more difficult to interpret. Here and to the east, the pattern appears remarkably smooth and uniform, with a clear direction along the major axis of the filament for the field over MM2-*F*, but turning to $\sim$45° between MM2-*B* and MM2-*D*. This uniformity strongly suggests that magnetic tension along the filament is

dynamically significant. The width of this emission is about half the filament width, or 3.″2, which is about 0.08 pc. However, to the west, the field lines deviate ∼40° and are even orthogonal to the main axis in some parts. Continuity in the field lines is present as the field smoothly changes direction. This change is significant, and it occurs across an important section of the filament. In Figure 2 we see that the width of the 5σ pseudo-vectors that change direction in region 2 is about 1.″4, or 0.04 pc. Thus, the field appears to have a coherent and smooth direction over many core length scales, which suggests that the field is not affected by the gravitational pull of these cores. In region 3, the field lines approximate a radial pattern over core *B*. However, the significance of the emission is not as high as over core *A*, and thus this interpretation is inconclusive. To the east of core *B* we have almost negligible polarized emission at a Stokes *I* level, where we do detect polarized emission elsewhere (region 4). At the eastern edge of region 3, the field lines appear to follow the main axis, but they smoothly deviate below core *B* to become orthogonal to the main axis of the filament. It is not clear how the field connects from the eastern edge of region 3 with the field in region 2 given the deviation we see. In region 4 the polarized emission is not as significant, and the required number of points to estimate the field was met by considering the 2.5σ pseudo-vectors. Nevertheless, the field morphology seems consistent with the more significant points. The inferred field lines in this region appear to connect with the field in the main filament. It is clear that the field evolves from being orthogonal to the main axis of the filament to a smooth alignment with the main axis.

3.2.2. The W43-MM3 Field

The magnetic field morphology over the MM3 clump, shown in Figure 3, is distributed mostly throughout the center of the filament. It shows four distinct regions that include all the detected cores in the clump, where the field appears to be well ordered. Although the polarized emission appears to be more compacted than in MM2, there is also indication of continuity from region to region in the derived field morphology. In all of these four regions, we have a sufficient number of independent points to estimate $B_{\rm pos}$. These distinct regions are also indicated in Figure 9 and the estimates for $B_{\rm pos}$ and the parameters from the polarization map are listed in Table 4. Most of the polarized emission is located around cores *A*, *B*, and *D* (region 3) at the center of the filament, and over core *F*, where the polarized emission is the brightest in the clump. Over MM3-*A*, the field morphology appears similar to what we have seen in MM2 and MM1, where the field appears to be dragged by gravity. Following the discussion for the MM2 field strength estimate over region 1, the EVPA dispersion seen over region 3 in MM3 also appears to result from perturbations by infalling gas over the field lines rather than turbulence. Therefore, we also consider the estimates here to be lower limits, with estimated values for $B_{\rm pos}$ of between 0.1 and 1.4 mG.

The polarized intensity map from the MM3 clump (Figure 3) shows strong and compact emission (up to 30% of Stokes *I*) around and over core *F*. The inferred magnetic field morphology is uniform and ordered, with a small dispersion in the field lines orientation (i.e., equivalent to the EVPA dispersion, or $\delta\phi = 10.^{\circ}3$). A similar situation is seen over core *C* and to a lesser degree over *E*, where the polarized emission is compact but not as strong as what is seen over core *F*. However, we do not detect polarized emission over the shell associated with the UC H II region. Given the size and flux obtained from the shell, we would have expected to detect polarization at similar levels as in the other regions in the clump (see the regions defined in Figure 9). We explore possible explanations to this in Section 4.2.

We obtained significant values for $B_{\rm pos}$ in the order of milliGauss from all three estimation methods for all the regions in MM3. The range of the fractional polarization is also significant. We obtained from 0.5% to 30.7%, where most of the emission is on-axis with the exception of region 1, which is located at the edge of the one-third of the primary beam (see the inner dotted circle in Figure 3) and slightly off-axis. The 0.5% correspond to region 3 and over core *A*, which is expected given the increase in the Stokes *I* emission due to the larger column density. This tendency of lower polarization fraction with increasing column density has been commonly observed (Fissel et al. 2016). In contrast, the highest amount of fractional polarization comes from compact and bright spots of polarized intensity. It is not clear why we see such a compact clusters of polarized emission (see also results for MM6 and MM7), but it might correspond to places where the dust its well illuminated by the radiation field produced by the protostars, or some other source, which might significantly increase the grain alignment.

3.2.3. The W43-MM4 Field

In the case of the MM4, the polarized intensity is confined to the center of the clump and around core *A*. Polarized emission is also detected to the northwest over core *E* and to the southwest, but there we did not detect cores with sufficient significance. All the detections are on-axis, as indicated by the inner dotted circle in Figure 5. The inferred magnetic field morphology is remarkably uniform, suggesting almost parallel field lines over cores *A* and *F*. The extension of the detected field is about 4″, or 0.11 pc. Although it is difficult to conclude whether MM4 is a filament given its compact morphology, it is possible to define a major axis southeast to northwest (see Figure 5), which seems to be orthogonal to the main field direction. Over core *E* and to the southwest tail from core *A* (a tail that seems orthogonal to the defined main axis), the field lines are also parallel, but the number of independent points is too small to reliably estimate the field. Nonetheless, over core *E*, the EVPA uniformity is significant with a small dispersion estimate ($\delta\phi \sim 5^{\circ}$), which suggests a strong field. Toward cores *C*, *G*, and *D*, we did not detect significant polarization. Only a compact amount of polarized intensity, at a level of 10%, is detected at the edge of core *C*. We estimated $B_{\rm pos}$ toward the center of the MM4 clump, where we obtained strengths on the order of milliGauss (<10 mG, see Table 4).

The position of the associated UC H II region in W43-MM4 is not obvious from our map. As a difference with MM3, we did not find IRAC counterparts, but nevertheless, this suggests that the MM4 clump is in a more evolved state of evolution than some of the other clumps (e.g., MM2). Given that the sizes of UC H II regions are expected to be small and <0.1 pc (Tan et al. 2014), the UC H II region is likely unresolved in our data. Although an H II region will expand more easily along the field lines, it is difficult to ascertain if the UC H II region has a significant impact in the magnetic field, as the field coherent scale is larger than the expected size of the UC H II region. Nevertheless, here we found striking differences in the polarized emission between two clumps where UC H II regions

have been detected. In MM3, we found no polarized emission at all around the area where the UC H II is detected, but in MM4, we found a significant amount of polarized emission. A possiblity is that in MM4 we see a still unperturbed envelope of gas and dust, while in MM3 a cavity has already been formed by the UC H II region. Accretion from infalling motions is difficult to establish in MM4. Although the line profile from the $HCO^+(3 \rightarrow 2)$ suggests self-absorption, we do not have confirmation from $H^{13}CO^+(3 \rightarrow 2)$ as the line appears to be optically thick (see Figure 4 in Motte et al. 2003).

When we compare the MM4 clump to other objects, it seems similar to the W3-Main IRS 5 clump, which has been resolved into at least five cores, although the column densities are lower ($\sim 10^{-23}$ cm^{-2}, according to Rivera-Ingraham et al. 2013). Hull et al. (2014) imaged W3-Main in 1 mm polarization with CARMA, obtaining a sufficient magnetic field map. There map shows a field morphology over IRS 5 that resembles an hour-glass shape, which is different from the field morphology of MM4. However, to the west of IRS 5, the field morphology seems relatively smooth, with parallel field lines to the south. Hull et al. (2014) associated this emission with the free–free emission from the W3-B H II region, which is also associated with an infrared source (IRS 3) that has been resolved into a type O6 star (IRS 3a). As free–free emission is very weakly polarized (<1%), the polarization pattern seen in both W3-Main and MM4 cannot be explained in this way. Thus, grain alignment seems the only possibility to explain the polarized emission, which might be coming from the envelope around the UC H II region. The line of magnetic force tends to remain straight when density irregularities develop (Spitzer 1978), which might be interpreted as field lines becoming more ordered through compression (as seen in the low-mass star-forming core B335; Maury et al. 2018).

3.2.4. The W43-MM6, MM7, AND MM8 Fields

The MM6, MM7, and MM8 clumps show significantly less amount of polarized emission than the previous clumps. Although the MM6 and MM8 clumps are in the lower range of masses in our sample, the dust continuum emission from some of their cores is comparable to cores in the other clumps where we did detected polarized emission. However, the amount of polarized emission seen in their maps appears negligible (see Figures 6–8, and 18). Thus, we did not attempt to estimate $B_{\rm pos}$ for these sources. What seems to be common in all these clumps (including the whole sample), is the presence of strong and compact sources of polarized intensity. This is clearly seen in MM6 core *B*, where the polarized emission is confined, just, to that core. We will explore this further in the discussion (see Section 4.2). On the other hand, the MM7 clump has a sufficient number of points to estimate $B_{\rm pos}$ over core *K* (if we consider the 2.5σ values, see Figure 7). Here, we obtained magnetic field strengths around 1.7 mG considering the average from all three methods. The maximum fractional polarization is also high and about 19% which suggests an increase in grain alignment efficiency.

3.3. Line Emission

3.3.1. Line Emission from W43-MM2

Molecular line emission from high-density tracers was also mapped toward the MM2 and MM3 clumps. Figure 10 shows the single-dish ASTE $HCN(J = 4 \rightarrow 3)$ and $HCO^+(J = 4 \rightarrow 3)$ spectra toward the center of MM2, along with their respective Gaussian fits. Both molecules show a dip in their line profiles at $\sim$91 km s^{-1}, which is suggestive of self-absorption. In the absence of molecular emission from an optically thin species tracing similar densities (e.g., $H^{13}CO^+(J = 4 \rightarrow 3)$), we use the published $H^{13}CO^+(J = 3 \rightarrow 2)$ from Motte et al. (2003) spectra to confirm the self-absorption. A line center velocity of $V = 90.8$ km s^{-1} was derived from the $H^{13}CO^+(J = 3 \rightarrow 2)$ spectrum, which is consistent with the dip in the $HCN(J = 4 \rightarrow 3)$ and $HCO^+(J = 4 \rightarrow 3)$ spectra (see Figure 10 here and Table 2 in Motte et al. 2003). In fact, this velocity is used as the $V_{\rm lsr}$ of MM2. Now, our Gaussian fitting results show two components centered at 89.7 and 93.2 km s^{-1} with amplitudes of 1.4 and 0.99 K for the HCN line; while for the HCO^+ line, the two components are found at 88.4 and 93.4 km s^{-1} with amplitudes of 0.7 and 0.4 K, respectively. When we compare the two components to the $V_{\rm lsr}$, the blue asymmetry is clear because the blue component from both lines has a much higher intensity than the red component. This type of profile is suggestive of infalling motions (Leung & Brown 1977). Figure 11 shows $HCN(J = 4 \rightarrow 3)$ spectra around the reference coordinates covering and area of $44'' \times 44''$ sampled every $10''$. The blue asymmetry is present in all spectra throughout MM2. We explore the implications of this blue asymmetry below (see Section 3.4).

3.3.2. Line Emission from W43-MM3

Figure 10 also shows the $HCN(J = 4 \rightarrow 3)$ and HCO^+ $(J = 4 \rightarrow 3)$ spectra toward the same coordinates we used as phase center for MM3. As with MM2, the emission is also suggestive of self-absorption, although the HCN line does not present a strong dip in between components and is also broader and noisier than the HCO^+ spectrum. For MM3 we also used the $H^{13}CO^+(J = 3 \rightarrow 2)$ results from Motte et al. (2003), which yielded $V_{\rm lsr} = 93.5$, consistent with the dip seen in the spectra. We also created a $44'' \times 44''$ grid around the MM3 reference coordinates to search for blue asymmetry in the spectra as was done for MM2. However, in this case, we found that only spectra $\delta\alpha = 0''$ and $\delta\alpha = 10''$ show a blue asymmetry, while the spectra with $\delta\alpha = -10''$ show a red asymmetry in both $HCN(J = 4 \rightarrow 3)$ and $HCO^+(J = 4 \rightarrow 3)$ emission (see Figure 12). This may indicate rotation in the MM3 clump at large scales.

3.4. Infalling Motions

Historically, asymmetries found in the spectra of molecular lines have been used to probe for infalling motions in star-forming cores. Leung & Brown (1977) suggested that an asymmetry in the line profile toward the blue may indicate the presence of infalling motions. Thus, the low-excitation and redshifted infalling layers of gas in the front part of the cloud absorb some of the emission from the rest of the gas. This redshifted self-absorption causes the spectrum to show a brighter blue peak. To quantify this asymmetry, we computed the normalized velocity difference from our data as explained in Appendix B.

We calculated $\Delta V_{\rm be}$ for the $HCN(J = 4 \rightarrow 3)$ and $HCO^+(J = 4 \rightarrow 3)$ spectra coming from the center of both MM2 and MM3 (see Table 2), as well as the $H^{13}CO^+$ $(J = 3 \rightarrow 2)$ previously used to check for self-absorption. The

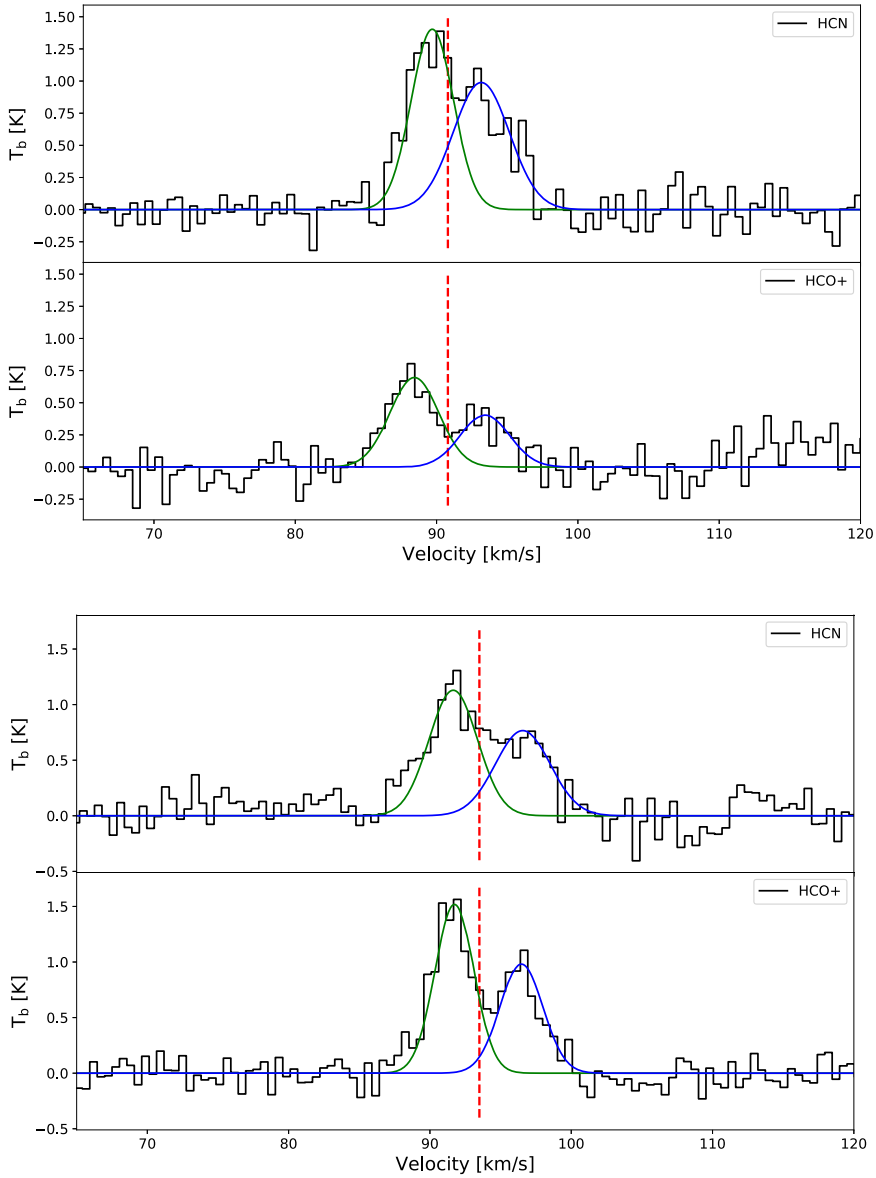

Figure 10. The HCN($J = 4 \rightarrow 3$) and HCO^+($J = 4 \rightarrow 3$) spectra from the MM2 (*upper panel*) and the MM3 (*lower panel*) clumps. The spectra correspond to observations of the clump phase centers obtained with ASTE. The red dashed line corresponds to the $V_{\rm lsr}$ of those clumps as obtained from the $H^{13}CO^+$($J = 3 \rightarrow 2$) spectral from Motte et al. (2003). In blue and green we show the Gaussian fits over the line components.

$\Delta V_{\rm be}$ values obtained for both MM2 and MM3 from the HCN and HCO^+ emission are all suggestive of infalling motions. These values are less pronounced than results obtained toward MM1. Cortes et al. (2010) computed the $\Delta V_{\rm be}$ using same molecular transitions, obtaining values ~ -1 (see Table 3 in Cortes et al. 2010).

To characterize these infalling motions, we applied a simple infalling model, as also described in Appendix B. We first fit a double Gaussian to the HCN and HCO^+ spectra from the center of clumps MM2 and MM3. The Gaussian fitting is shown in Figure 10. The model was then adjusted to the resulting Gaussian spectra by minimizing the χ^2 function through the Levenberg–Marquardt algorithm (Press 2002). The fit parameters are presented in Table 5. The infalling model implicitly assumes accretion onto a protostellar object. The two layers that define the model are assumed to have an infalling direction onto a single core. By modeling infalling motions in this way, it is possible to estimate the infalling speeds by averaging both the front and rear components, as listed in Table 5 for MM2 and MM3. For MM2 and MM3, the infalling speeds obtained from HCN and HCO^+ are comparable within 70%. Using these infalling speeds and assuming spherical geometry, we estimate the mass infalling rate for these clumps by calculating

$$\dot{M} = \frac{dM}{dt} \sim \frac{M}{t} = \frac{\rho V v_{\rm in}}{R} = \frac{4}{3}\pi n_{\rm H_2}\, \mu m_{\rm H} R^2 v_{\rm in}, \qquad (3)$$

where $\mu = 2.35$ is the mean molecular weight, $R = 0.3$ pc is the geometric radius, and $n_{\rm H_2}$ is the gas number density taken from Table 3. The results are listed in Table 5. The blue asymmetry in the line shape is more clearly visible in the HCO^+ emission, therefore we only considered those results to estimate $\dot{M}$. Therefore, we obtained a mass infall rate of

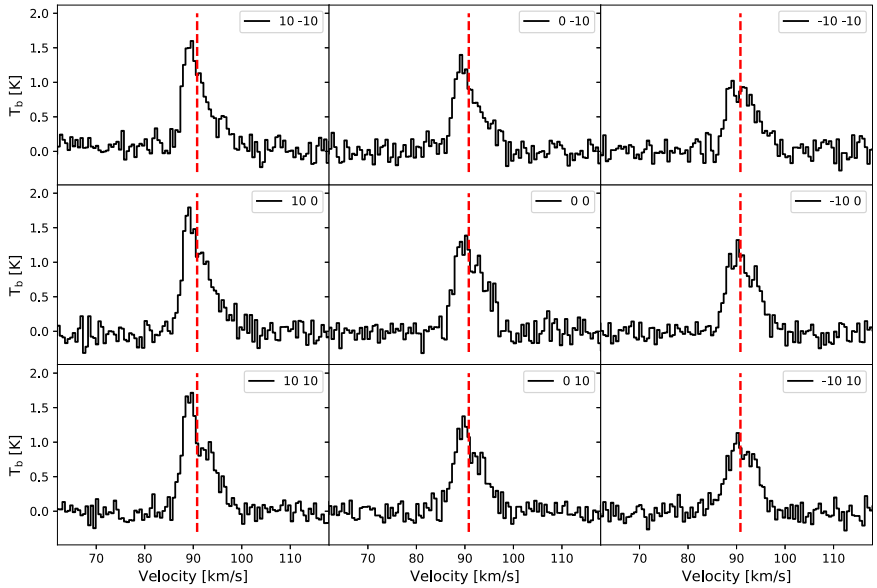

Figure 11. Here we show a 3 × 3, 10″ spaced HCN($J = 4 \rightarrow 3$) panel from the MM2 clump. In red we show $V_{\rm lsr} = 90.8$ km s^{-1}. The labels correspond to the offsets with respect to the center coordinates, which is also the sampling rate used for the OTF mapping made with ASTE over the MM2 clump.

$\dot{M} = 1.8 \times 10^{-2}\, M_\odot\, {\rm yr}^{-1}$ for MM2 and $\dot{M} = 6.3 \times 10^{-3}\, M_\odot\, {\rm yr}^{-1}$ for MM3. In principle, we expect that the HCO^+ emission is diluted in the ASTE 22″ beam, and to estimate the infalling radius, we therefore used the dust emission as a proxy. Although it is not clear that the dense molecular gas will follow the spatial distribution of the dust emission, this will still give a better estimate than deriving the radius from the ASTE beam. Our interferometric maps of MM2 and MM3 have a maximum recoverable angular scale of about 0.3 pc, and thus, these ALMA data are insensitive to length scales larger than this. Given this limitation, we have assumed 0.15 pc as the radius for estimating the infalling mass rate. This is reasonable given the geometric assumptions we used here. Cortes et al. (2010) estimated the mass infall rate for MM1 assuming a radius derived from interferometric observations obtained with the BIMA array at a much coarser resolution. Here we also refine this calculation using the same assumption for the radius, and also updating the mass density to $n_{\rm H_2} = 10^6\, {\rm cm}^{-3}$, which gives us a mass infall rate for MM1 of $1.3 \times 10^{-2}\, M_\odot\, {\rm yr}^{-1}$. These infall rates are consistent with previous estimates for MM1 (Herpin et al. 2009), and results obtained toward other high-mass star-forming regions by similar analysis (Saral et al. 2018) and by radiative transfer modeling and SED fitting (Fazal et al. 2008).

4. Discussion

4.1. The Dynamical Equilibrium of Cores in the W43-Main Clumps

4.1.1. Initial Considerations

We detected 81 cores in our sample of clumps in W43-Main. Most of these cores are located along the main axis of their respective filaments, but some exceptions, corresponding to isolated cores, are seen outside the main filaments. The estimated core masses range from a few to ~426 $M_\odot$, where only 2 marginally subsolar cores were detected.[19] The spatial distribution of cores in all clumps is suggestive of clusters or associations. However, a significant number of cores, 54 objects, or 66%, have masses below 10 $M_\odot$, which is suggestive of low-mass star formation. A similar situation has also been described for W43-MM1 (see Paper I and Motte et al. 2018). Additional examples from other high-mass star-forming regions have been presented in the literature (Frau et al. 2014; Zhang et al. 2015; Cyganowski et al. 2017; Sanhueza et al. 2017; Lu et al. 2018). This indicates that low-mass stars are also being formed along with high-mass stars, and therefore, low- and high-mass star formation processes might be coupled.

Understanding the dynamical equilibrium of protostellar cores is required to assess whether these cores are collapsing and forming stars or if they are still unbound. We do this by considering the contributions from thermal motions, nonthermal motions (turbulence), and magnetic fields, as the most important physical parameters against gravity. Rotation at the core scales might be relevant, especially if flattened structures (disks?) have formed. However, it has been found that in low-mass star-forming clouds, rotation does not seem to provide significant support against gravity at the length scales traced by our data (Tobin et al. 2012). Therefore, and given the lack of detailed kinematical information from our observations, we do not consider rotation here. Additionally, previous studies suggest that magnetic fields play a role in the level of fragmentation within a core, although this is still debated (Palau et al. 2013, 2015).

We understand that a core is collapsing if the estimated mass is higher than some critical mass by the application of virial equilibrium. The considerations behind determining this critical mass has been the subject of a number of works in the past (Spitzer 1978; Bertoldi & McKee 1992; Shu 1992). It is often found that the virial mass was determined by only considering

[19] The significance of these subsolar cores is $\sim 10\sigma_M$ given a mass sensitivity of $\sigma_M = 0.08\, M_\odot$.

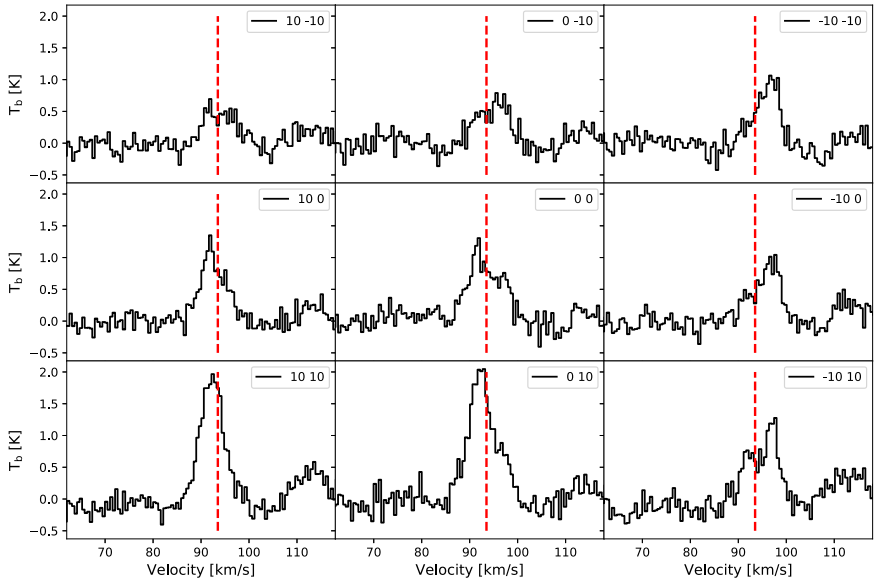

Figure 12. Here we show a 3 × 3 10″ HCN($J = 4 \rightarrow 3$) panel from the MM3 clump. In red we plot $V_{\rm lsr} = 93.5$ km s^{-1}. The labels correspond to the offsets with respect to the center coordinates, which is also the sampling used for the OTF mapping made with ASTE over the MM2 clump. Although the profiles suggest a blue asymmetry in most of the spectra, to the west there is a clear red asymmetry, which may suggest rotation at the clump scales. Additionally, there is some indication of high-velocity emission at about 115 km s^{-1} in some of the spectra.

the gas kinematics, thermal and nonthermal (turbulence), and sometimes, by considering "reasonable" estimates of the magnetic field strength. However, in this work we do have quantitative information about the magnetic field and can therefore include more accurate estimates of its strength in the calculation. We start by computing what in the literature is referred to as the virial mass, or $M_{\rm vir}$. As this mass is a representation of the energy contained in both thermal and nonthermal motions, we refer to it here as the kinetic mass, which we calculate as

$$M_{\rm kin} = 3k\frac{R\sigma_{\rm v}^2}{G}, \tag{4}$$

where R is the core radius, $\sigma_{\rm v}$ is the gas velocity dispersion along the line of sight, which is derived from the molecular line width as $\sigma_{\rm v} = \Delta V_{\rm FWHM}/2\sqrt{2\ln 2}$, G is the gravitational constant, and k is a correction factor introduced by MacLaren et al. (1988) to account for the a power-law density profile $\rho \sim R^{-a}$. Assuming a constant density in the condensation, or $a = 0$ and $k = 5/3$, the kinetic mass can be rewritten as

$$M_{\rm kin} = 1.17\left(\frac{R}{\rm mpc}\right)\left(\frac{\sigma_{\rm v}}{\rm km\ s^{-1}}\right)^2 M_\odot. \tag{5}$$

The gas kinetic energy is represented by the nonthermal motions seen from the molecular line widths, which are here midly larger than the thermal sound speed. Here, we use the same line widths we used to estimate $B_{\rm pos}$, but at core scales of 1″, which are about the average of our core sizes (see Section 3.2 and Appendix A). For completion, we also calculated the Jeans mass, $M_{\rm J}$, for each core. The computed values for $M_{\rm J}$ and $M_{\rm kin}$ are shown in Table 3. The kinetic mass already includes the contributions from thermal and nonthermal energy to the balance equation. To assess the support provided by motions against gravity, we use the kinetic mass to define a kinetic virial parameter, $\alpha_{\rm kin} = M_{\rm kin}/M_{\rm gas}$ (Bertoldi & McKee 1992).

To quantify the contribution from the magnetic field in the balance against gravity, we define the magnetic mass as $M_\Phi = \Phi/2\pi G^{1/2}$ (Nakano & Nakamura 1978; Crutcher et al. 2004), where Φ is the magnetic flux and G is the gravitational constant. We used this definition to be consistent with the mass-to-magnetic flux ratio definition (see paragraph below). Having defined $M_{\rm kin}$ and M_Φ, we can now calculate a total virial parameter as

$$\alpha_{\rm total} = \frac{M_{\rm kin} + M_\Phi}{M_{\rm gas}}. \tag{6}$$

The $\alpha_{\rm total}$ includes the contribution of the magnetic field in the ratio by adding the magnetic field mass. In this way, we account for all the relevant physical processes that oppose gravitational collapse.

To explore the magnetic-only contribution, we compute the mass-to-magnetic flux ratio, as done before in W43-MM1 (Paper I). We do this to compare the relevance of the magnetic field with respect to gravity. The mass-to-magnetic flux ratio is defined following Crutcher et al. (2004)

$$\lambda_B = \frac{\langle (M/\Phi)_{\rm observed}\rangle}{(M/\Phi)_{\rm crit}} = 7.6\times 10^{-21}\frac{N({\rm H_2})}{3B_{\rm pos}}, \tag{7}$$

where $N({\rm H_2})$ is the molecular hydrogen column density in cm^{-2} calculated for each source independently, $B_{\rm pos}$ is the magnetic field strength in μG assumed to be a global physical parameter for a given region (see Section 3.2 for a description of the chosen regions), where the factor of 3 in the denominator corresponds to an statistical geometrical correction for $(M/\Phi)_{\rm observed}$. The geometrical shape of a core depends on the strength of the magnetic field, which will tend to flatten the core along its minor axis. In the limit case of a strong magnetic field, the core might converge to a pseudo-disk (Mouschovias 1987). Table 4 presents

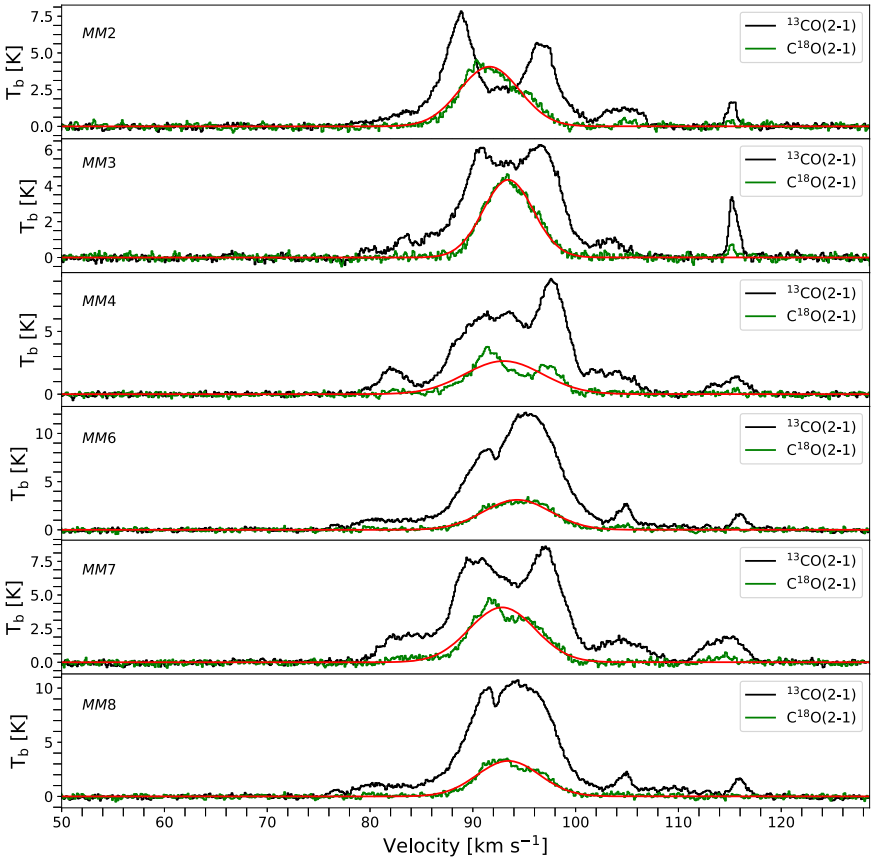

Figure 13. We show ^{13}CO($J = 2 \rightarrow 1$) in black, and C^{18}O ($J = 2 \rightarrow 1$) spectra in green. The data were extracted from the public survey reported by Carlhoff et al. (2013) using circular regions of 10″ in diameter centered at the coordinates of the most massive cores of each clump detected in this work. Superposed in red is the Gaussian fit to the C^{18}O ($J = 2 \rightarrow 1$) line. The name of each clump is indicated in the insets.

Table 1
The Line Parameters for ASTE Molecular Line Observations

Line	Transition	Frequency (GHz)	Map Size (arcsec^2)	rms-noise (K)
HCO^+	($J = 4 \rightarrow 3$)	356.7342880	200″ × 160″	0.83
HCN	($J = 4 \rightarrow 3$)	354.5054773	200″ × 160″	0.83

Table 2
Normalized Velocity Difference

Clump	Line	ΔV_{be}
MM2	HCN($J = 4 \rightarrow 3$)	−0.3
MM2	HCO^+($J = 4 \rightarrow 3$)	−0.6
MM3	HCN($J = 4 \rightarrow 3$)	−0.4
MM3	HCO^+($J = 4 \rightarrow 3$)	−0.4

Note. The asymmetry in line profiles is presented by calculating ΔV_{be}, as shown in Equation (12), where the optically thin species correspond to $H^{13}CO^+$. The values used to compute the blue excess are taken from Gaussian fits to the corresponding spectra.

the derived values for λ_B using all three B_{pos} estimations. Although the nomenclature might appear confusing as λ_B is essentially M_{gas}/M_Φ, which is the inverse of a magnetic α parameter, we have decided to keep it in order to be consistent with the literature.

4.1.2. Caveats

Before stating the result of our computations, it is necessary to factor in the uncertainties in the calculation. We derive velocity dispersions by assuming a Kolmogorov-like power spectrum, which we believe is representative of the nonthermal motions induced by the turbulence cascade from the large scales, although its nature is uncertain. Furthermore, this assumption makes the calculation of the kinematic mass (see Section 4.1.3) independent of the temperature. However, turbulence can be injected at smaller scales by outflows, shocks, and ionization fronts, and winds coming from the newly born stars, none which we consider in this analysis. Nevertheless, magnetic fields have a dampening effect on turbulence at small scales, which might decrease the contribution to the turbulent energy close to the core scales. This is also suggested by magnetohydroynamcis (MHD) simulations, where the velocity dispersion in gravitationally bounded cores was found to be sonic or mildly supersonic (Hennebelle 2018). Therefore, the injection of additional energy into the turbulence at these length scales should happen continuously to alter the energy cascade and to modify the velocity dispersion significantly. Also of importance are the uncertainties in the mass estimation. The mass estimates depend on the dust temperature, a proxy for the gas temperature, which is not well constrained for these clumps. High-mass protostellar cores are seen to develop hot cores quite early in their evolution, although the exact process is unclear. In W43-Main, the binary in MM1-*A* has already developed a hot core (Sridharan et al. 2014). An increase in the inner core temperature will decrease

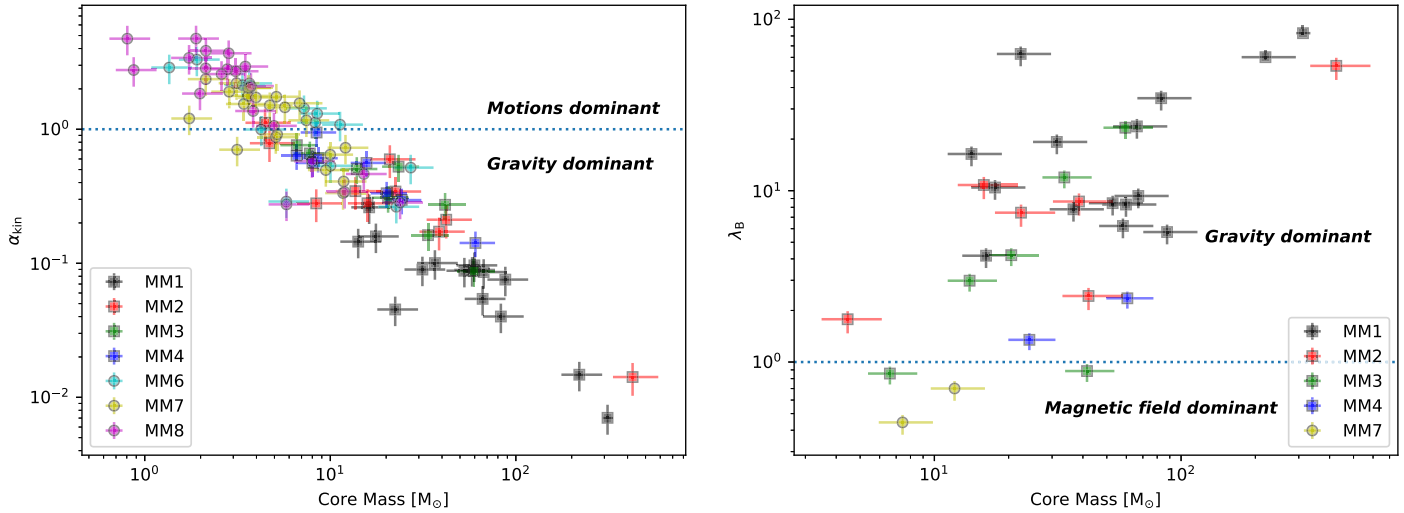

Figure 14. Here we show the α_{kin} virial parameter (*left*) and the mass-to magnetic flux ratio, or λ_B (*right*), as a function of core mass in $M_\odot$. The cores are colored according to their clumps, as indicated by the label. Error bars are displayed for the mass, λ_B, and α_{kin} values computed by using a range of three temperatures for all cores in each clump (see the discussion in Section 4.1.3). The blue dotted line corresponds to the critical threshold in the virial equilibrium.

the mass estimate and therefore increase the α_{total} ratio, which might alter the conclusions. However, this is difficult to address without better spectroscopic millimeter or submillimeter data from these cores. Additionally, all three B_{pos} estimations require the volume number density as an input, which we computed by assuming spherical geometry. This assumption might bias the B_{pos} computation toward higher values, especially if the geometry in the line of sight has a flatter shape.

4.1.3. The Virial Equilibrium

We first compare turbulence and magnetic fields independently against gravity. For thermal energy, all cores in our sample show Jeans masses that are orders of magnitude lower than the core estimated mass, as shown in Table 3. It is clear at this point that thermal pressure on its own does not contribute significantly as a support mechanism against gravitational collapse at this stage in the evolution of our cores.

When considering support from kinetic energy alone, we found that 43 out of 81 cores have $\alpha_{kin} < 1$ (as shown in Figure 14). This corresponds to most of the cores from MM2, MM3, and MM4, and with some additional cores from the other clumps. Values of $\alpha_{kin} < 1$ suggests that turbulence alone cannot support these cores against gravity. An extreme case is MM2-*A*, which is 2 orders of magnitude away from virial equilibrium. In contrast, the cores with $\alpha_{kin} > 1$ belong mostly to MM6, MM7, and MM8 with just one core from MM2, suggesting that these cores are gravitationally unbound. This set of cores belong to the low-end range of the mass distribution and also to the clumps with the highest degree of fragmentation (clumps MM7 and MM8).

Considering that we have detected large-scale infalling motions, we would have expected to see most of these cores with $\alpha_{kin} < 1$. However, in ∼47% of our cores the energy from turbulence alone seems sufficient to support the cores against gravity. Although transient cores, due to the turbulence energy cascade, cannot be immediately ruled out, the high column densities obtained (mostly in excess of 10^{24} cm^{-2}) suggest that these cores are likely pressure confined, and thus the most likely scenario is that these cores are still accreting gas, but have not yet reached a critical mass to ensure gravitational collapse.

To consider the magnetic-only contribution to the virial analysis, we calculated λ_B only for the cores with associated B_{pos} estimates (see Figure 14 and Table 4). We computed λ_B using the average of all three B_{pos} estimates. Our results show that most of the cores from MM2, MM3, MM4, and MM7 with B_{pos} estimates are supercritical, particularly MM2-*A*, *B*, and MM3-*A*, *B*. Two cores from MM3 (MM3-*E* and MM3-*F*) are sightly subcritical, and two from MM7 appear to be subcritical (MM7-*H* and MM7-*K*). However, for MM2-*A*, MM2-*D*, MM3-*A*, MM3-*B*, and MM3-*D*, the values for λ_B are upper limits given that the magnetic field estimates are lower limits (see Section 3.2). For the supercritical cores, the interpretation is that the magnetic field by itself does not provide sufficient support against gravity, and therefore they should be out of virial equilibrium unless additional sources of energy (turbulence) can further contribute to the core support. For the subcritical cores, the results suggest that the magnetic field alone might be supporting these cores against gravity. Although the two cores in MM3 have large differences in the mass estimates, the magnetic field morphology that surrounds them shows almost no dispersion in the EVPA, resulting in strong B_{pos} estimates (of $\langle B^{F}_{pos}\rangle = 4.2$ mG and $\langle B^{E}_{pos}\rangle = 5.5$ mG). Frau et al. (2014) investigated NGC 7538, IRS 1-3, with the SMA, where they found a number of low-mass cores along the spiral arms of the filament that also appear to be subcritical. These cores are also at the low-end of their mass distribution.

Finally, we consider both turbulence and magnetic energy in the dynamical equilibrium of the cores in W43-Main by computing the total virial parameter α_{total} as a function of the estimated core mass (see the left panel in Figure 15). From a total of 17 cores, we found 5 objects, or 29%, with $\alpha_{total} > 1$. The remaining 12 cores, or 71% of the total, have $\alpha_{total} < 1$ and should be out of virial equilibrium. Here, out of virial equilibrium implies that as we are accounting for all the relevant physical parameters at these length scales, these cores should be self-gravitating and forming stars. The final multiplicity inside each core is unclear from these data, and only observations with higher resolution might provide answers to this question. Although the number of bound cores dominates the distribution, the evidence from B_{pos} estimates coming from

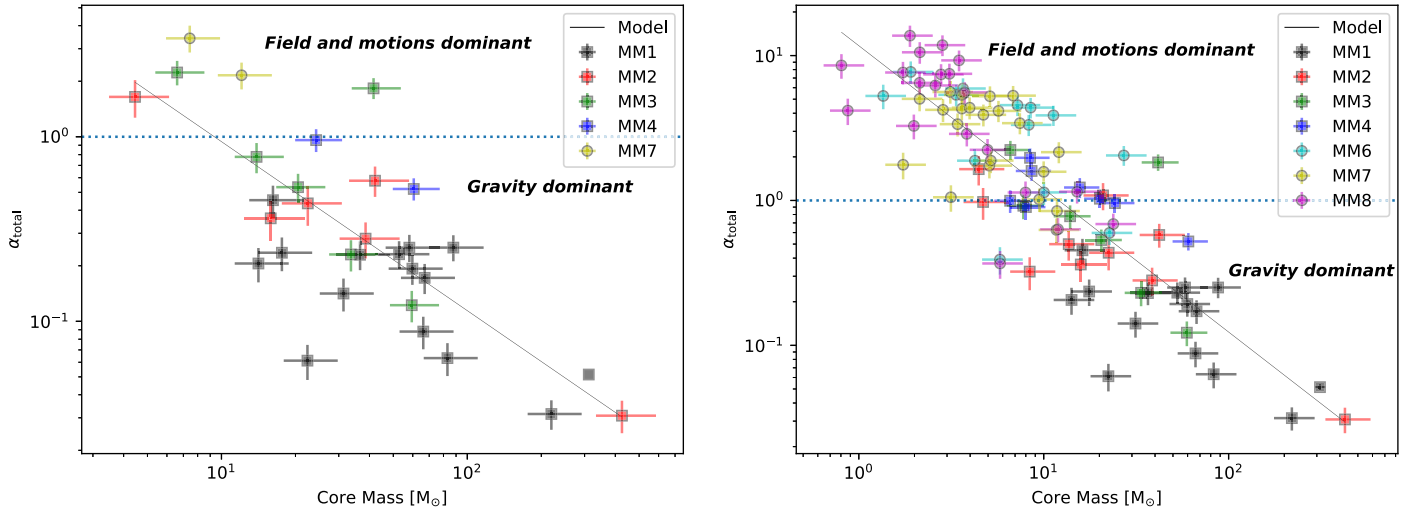

Figure 15. Here we show the total virial parameter, or α_{total} (*left*), for the sample of cores where we derived B_{pos} estimates directly from the data, and the α_{total} parameter when all cores are considered (*right*). Both panel show plots as a function of core mass in $M_\odot$. The cores are colored according to their clump, as indicated in the inset. Error bars are displayed for the mass and α_{tot} estimates computed using a range of three temperatures for all cores in each clump (see Section 4.1.3 for a discussion). The blue dotted line corresponds to the critical threshold in the virial equilibrium. The black line corresponds to the best power-law fit to α_{total}.

real data as well as reasonable velocity dispersions strongly suggests that the unbound cores are real. As previously stated, we also note that all of these cores are likely to be pressure confined given the high column densities observed toward these clumps. Thus, it is highly unlikely that the unbound cores are transient structures due to the turbulent cascade, and the more likely explanation is that these cores are still accreting and have not yet accumulated sufficient mass to become self-gravitating.

To increase our statistics, we estimated α_{total} for the totality of our cores by assuming "reasonable" B_{pos} values. We did this using proximity to regions with B_{pos} estimates, and in the case of MM6 and MM8, we used the average obtained from MM7 given the similarities in their fragmentation. The result of adding all of our cores is shown in Figure 15 (right panel). The figure shows two distinctive populations of bound and unbound cores. The bound cores belong to the population of the most massive clumps with direct evidence for infalling motions from large scales, although there a number of cores in a "critical" state. The unbound cores correspond to 70% of our sample, which although quite uncertain, strongly suggests that there is a population of cores that are not gravitationally bound. For this population of cores, the support against gravity comes from a combination of magnetic and turbulent energy. Although it is quite possible that the "reasonable" B_{pos} estimate used for MM7 and MM8 is large (we discuss this possibility in Section 4.2), any additional source of support will increase the unbound state of the cores that we have already seen from turbulence alone.

As previously discussed, a main uncertainty in our calculations might come from the temperature assumptions. Although the temperature we used to estimate the column density at each clump comes from SED derivations, these represent the large-scale structure within the clump (given the resolution of the single-dish telescopes used to derive these SEDs). Thus, the internal core structure, particularly in the most massive sources, might have temperatures that are higher than the nominal ones used here. To account for variation in the core temperatures, we calculated error bars for the mass, α_{kin}, λ_B, and α_{total}, using a ± 5 K temperature deviation relative to the nominal SED temperature of the clump. The temperature ± 5 K is a reasonable assumption for the bulk of the cores in our sample, although the more massive cores might have higher temperatures (as previously discussed). The spread shown by the uncertainty in the temperature slightly move the values, but the overall trend remains, as shown in Figures 14 and 15.

From ALMA observations of IRDC G28.34, Zhang et al. (2015) found 10 gravitationally bound cores and one clump, G28-P1, was found to be unbound. However, they did not have observational information about the magnetic field and thus, they assumed a value for $B = 270\ \mu$G in their analysis. Zhang et al. (2015) stated correctly that magnetic fields can substantially increase the value of the virial mass, which is exactly what we see in W43-Main. The values that we have estimated for the magnetic field are at maximum close to 2 orders of magnitude higher than the values used for G28.34, but biased toward the lower end because we used the region number density, which is lower than the core density (see Appendix A). The column densities derived toward the G28.34 cores, though not listed, appear to approach our results because the number density values are between 10^6 and 10^7 cm^{-3}. Given that density regime, it is likely that the field strength will be on the order of milliGauss for G28.34, as expected from observations (Crutcher 2012). This will certainly increase the virial mass for those cores, which might resemble what we see in W43-Main.

Having uncovered these two populations of cores in W43-Main, it should be noted that these populations will likely produce low- and high-mass stars. Thus, as some of these cores are gravitationally bound while the others are not, the timescale for star formation in these two populations has to be different. For the bound cores, collapse cannot proceed faster than the freefall time, which sets a lower limit. However, the unbound cores might be accreting at timescales set by the infall rate, which is substantially lower. This essentially suggests that the evolutionary timescale for star formation in high-mass filaments is not uniform.

Bertoldi & McKee (1992) derived a power law for the virial parameter in the form of $\alpha = b\left(\frac{M_o}{M_{obs}}\right)^a$ for magnetized

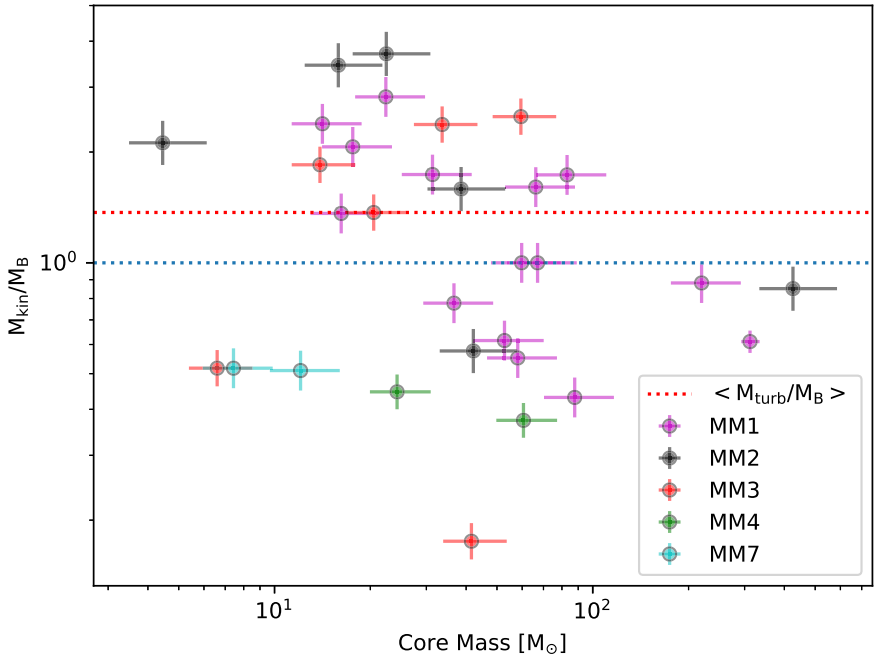

Figure 16. The ratio between the turbulence mass, or $M_{\rm kin}$, and the magnetic mass, or $M_{\rm B}$, as a function of core mass in $M_\odot$. Error bars are displayed for the mass and $M_{\rm kin}/M_{\rm B}$ ratio computed using a range of three temperatures for all cores in each clump (see Section 4.1.3 for a discussion). The blue dotted line corresponds to the equipartition threshold between the two physical parameters. The red dotted line marks the average for the ratio between $M_{\rm kin}$ and $M_{\rm B}$.

star-forming cores. To compare, we fitted our data with such a power law, obtaining $b = 1.06$ and $a = -0.92$ for the initial 17 cores and $b = 1.04$ and $a = -0.88$ for the whole sample (see Figure 15). Bertoldi & McKee (1992) derive $b = 2.12$ and $a = 2/3$ for magnetized critical clumps, and $b = 2.9$ and $a = 2/3$ for pressure-confined clumps. However, in their analysis they considered $M_O = M_{\rm J}$, which is different from what we use in $\alpha_{\rm total}$. In our case, $M_O = M_\Phi + M_{\rm kin}$, which might explain the difference. Frau et al. (2014) also fit a power law to their data, finding $b = 2.26$ and $a = -0.68$, in agreement with Bertoldi & McKee (1992), but they did not comment about the usage of the Jeans mass.

4.1.4. Comparison between Motions and Magnetic Fields

The virial parameter $\alpha_{\rm total}$, provides an assessment of the core equilibrium, but not information about the relevance of each of the parameters that counteract gravity. To explore the relative importance of kinetic energy and magnetic energy, we computed the ratio between the kinetic mass and the magnetic field mass (see Figure 16). The mean value for the ratio of the turbulent to magnetic field mass is $\langle M_{\rm kin}/M_\Phi\rangle = 1.43$, which suggests that turbulent energy dominates magnetic energy. Now, the Alfvén speed, $V_{\rm a} = B/\sqrt{4\pi\rho}$, has a range between $0.19 < V_{\rm a} < 2.9\,{\rm km\,s^{-1}}$, which is higher on average than the velocity dispersion, σ_B, as $\langle V_{\rm a}\rangle = 1.1 > \langle\sigma_B\rangle = 0.9\ {\rm km\,s^{-1}}$, if our assumptions are correct. This also suggests that magnetic tension in these filaments is strong and might dampen the turbulent cascade at these scales, unless turbulence is replenished. One way in which turbulence can be replenished is through outflow feedback. Figure 13 shows extracted ^{13}CO($J = 2 \rightarrow 1$) and C^{18}O ($J = 2 \rightarrow 1$) spectra from the W43-Main large-scale CO mapping by Carlhoff et al. (2013). Each spectrum was extracted from the clump phase center position and using pencil beam regions at the resolution of the IRAM telescope ($\sim$10″). The spectra shown in Figure 13 suggest that the ^{13}CO emission is optically thick at 1 mm, where there is also substantial structure in velocity for the points considered. Gaussian fits were made to the C^{18}O spectra (shown in red in Figure 13), which also suggests that in some clumps, C^{18}O might be optically thick. The emission at the line wings from ^{13}CO strongly suggests the presence of outflows in some of these clumps, and it is particularly clear in MM8 and MM6. Although ^{13}CO and C^{18}O trace more diffuse gas at 1 mm (the ^{12}CO, $J = 2 \rightarrow 1$, has a critical density $\sim 10^4\,{\rm cm^{-3}}$) than our dust emission, they are still a sufficient proxy for outflows.

4.1.5. On the Nature of MM2-A

The MM2-*A* core accounts for 73% of the total estimated mass for all cores in MM2. MM3-*A* corresponds to 30%, and MM4-*A* contributes 44% of the total mass for all the cores in both clumps. Although these are the most massive cores in our sample, MM2-*A* is by far the most massive core. In fact, MM2-*A* might be the most massive protostellar core in W43-Main now that MM1-*A* has been resolved into a binary (Motte et al. 2018). Because of this, and given that at the 0.01 pc scales MM2-*A* appears to be an unresolved and round protostellar core despite the elongated beam shape, it becomes interesting to understand how massive the resulting star might be. To estimate the final mass for a star in MM2-*A*, we follow Sanhueza et al. (2017), who made use of the Larson (2003) relation between the maximum stellar mass and the mass of the whole cluster, or

$$\left(\frac{M_{\rm max}}{M_\odot}\right) = 1.2\left(\frac{M_{\rm cluster}}{M_\odot}\right)^{0.45}, \quad (8)$$

here we derive the $M_{\rm cluster}$ from the MM2 total mass by making use of the current W43-Main star formation rate. For the MM2 mass, the current best estimate is $\langle M_{\rm MM2}\rangle = 4.4 \times 10^3\ M_\odot$ (Bally et al. 2010). Thus and assuming a star formation

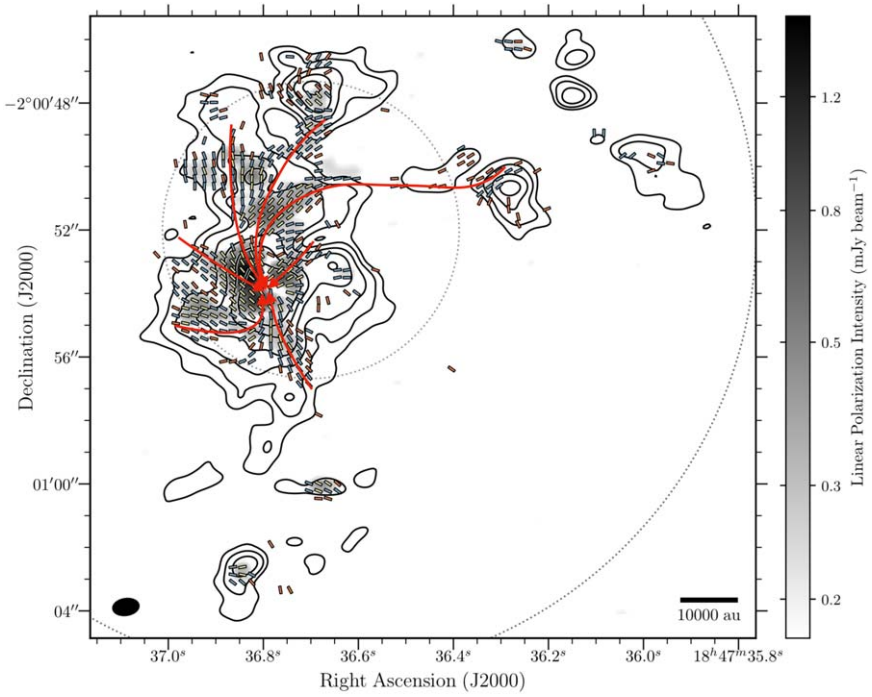

Figure 17. The magnetic field map in MM2 as shown by Figure 2. Superposed is a field line scheme as red arrows to illustrate the proposed field connectivity throughout the clump. Here we suggest that the magnetic field is connected and likely dragged into the gravitational potential well of MM2-*A*.

efficiency of 25% (Motte et al. 2003), we obtain $M_{\rm cluster} = 1.1 \times 10^3\,M_\odot$, which gives $M_{\rm max} = 28 \pm 14\,M_\odot$. The uncertainty in the mass estimates comes mostly from the temperature determination, which can introduce a 50% error in the estimation. Given the mini-starburst nature of W43-Main, the star formation rate may be higher than 25%, as estimated in other high-mass star-forming regions (Lada & Lada 2003; Alves et al. 2007). Thus, for a conservative increase to 30% in the star formation rate, we obtain $M_{\rm max} = 30 \pm 15\,M_\odot$. A $30\,M_\odot$ star will likely correspond to an O7 star, which is consistent with the spectral type of most of the stars in the W43 H II region (Blum et al. 1999; Heap et al. 2006). However, and as previously stated, the main caveat in the MM2-*A* mass estimation is the temperature assumption. As with MM1-*A*, it is possible that MM2-*A* has already developed a hot core inside, which will certainly increase the temperature and also decrease the mass estimate. Following Paper I, we also consider here $T = 70$ K to estimate the mass for MM2-*A*, which yields $M_A = 118\,M_\odot$. This mass estimate corresponds to 27% of the original estimate. Thus if we assume the same decrease in the maximum mass as previously obtained, we derive a $M_{\rm max} \sim 8\,M_\odot$. Although an $8\,M_\odot$ star is still a massive star, it is unlikely that MM2-*A* is a star like this. The current evidence suggests that accretion is still ongoing, and despite the temperature uncertainty, the final mass of the star might be close to the original estimate, or $30\,M_\odot$. It may very well be that the accretion timescale is longer than previously considered given the presence of strong magnetic fields.

Prestellar cores are the smoking gun for the core accretion model in high-mass star formation (McKee & Tan 2003). These cores should be massive, cold condensations ($T < 20$ K), where the emission is purely thermal. Thus, a high-mass prestellar core has not developed hot cores or outflows, and corresponds to the initial stage for high-mass star formation in the core accretion model. The MM2-*A* does not have a counterpart at 24 μm emission and radio continuum, which indicates a protostellar core in its earliest stages of evolution. Its massive gravitational potential well seems to be dragging the field throughout the clump and into core. We elaborate this proposal further by sketching the magnetic field connection in Figure 17. The red arrows indicate clump-scale field lines as they are dragged into MM2-*A*. It is unlikely that a massive core that can drag the field is in a prestellar phase. Although at a coarse resolution and lower sensitivity, the SMA has detected perturbed magnetic fields in both high and intermediate star-forming regions. Juárez et al. (2017) obtained a bimodal magnetic field distribution toward NGC 6334 V, which seems to converge toward a massive hot core. A similar situation is also seen in the DR21(OH) core, where the field also seemed dragged by gravity toward the core, although in this case the field appears to have a toroidal morphology as traced by SMA. Additionally, outflow emission from MM2-*A* can be explored from the ^{13}CO and C^{18}O spectra shown in Figure 13. The ^{13}CO spectrum from MM2-*A* at 0.27 pc scales (10″ angular scales) appears to show excess emission in both line wings, which resembles an outflow. The C^{18}O spectrum shows no excess emission in the line wings, but the line shape is not Gaussian and suggests some self-absorption, which makes the emission likely optically thick. Therefore, it is likely that MM2-*A* is not prestellar, but it might still be quite early in its evolution, and further studies at higher resolution will therefore hopefully uncover its nature.

4.2. The Polarized Intensity Distribution

A visual examination of the magnetic field maps from our clumps reveals differences in the amount and distribution of the polarized emission. For example, the MM2 clump has the most intense and most spread out amount of polarized emission, with

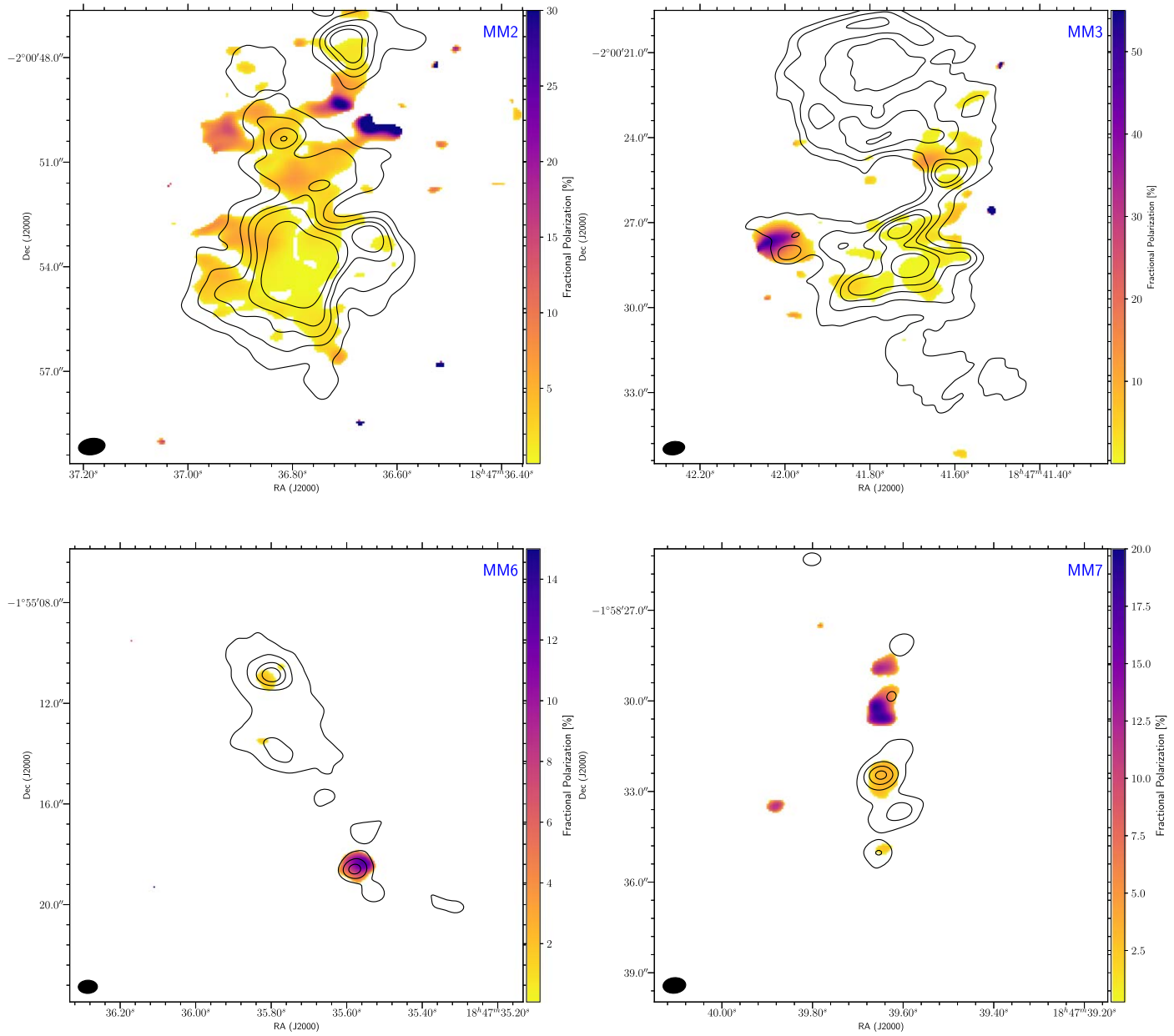

Figure 18. Fractional polarization for the MM2, MM3, MM6, and MM7 clumps as indicated by the blue label in the upper right corner of each panel. The fractional polarization map was calculated as the ratio between the polarized intensity map and the Stokes *I* map, but using only the values greater than or equal to $3\sigma_{\rm poli}$. Superposed to each fractional polarization map are Stokes *I* contours (10, 20, 33.3, 50, 100) $\times$ $\rm min_{poli}$, where $\rm min_{poli} = 5 \times \sqrt{\sigma_{poli}}$. The values for $\sigma_{\rm poli}$ are for each clump, $\sigma_{{\rm poli},mm2} = 5.9 \times 10^{-5}$, $\sigma_{{\rm poli},mm3} = 5.2 \times 10^{-5}$, $\sigma_{{\rm poli},mm2} = 5.3 \times 10^{-5}$, and $\sigma_{{\rm poli},mm2} = 5.6 \times 10^{-5}$, all in units of Jy beam^{-1}.

a peak intensity of 1.6 mJy beam^{-1} and an extension of 0.27 pc along the main axis of the filament. In contrast, the MM6 clump presents only compact and almost unresolved emission at two places in the filament (cores *A* and *B* in Figure 6). The peak polarized emission in MM6 is 1.1 mJy beam^{-1}, which is on the same order as the peak emission in MM2. The MM6 filament is almost twice the size of MM2 (with an extension of 0.42 pc along the main axis), but it is almost devoid of polarized intensity even at places where, from the Stokes *I* emission, we would have expected a detection (when compared to MM2). At the Stokes *I* lowest contour, which in both clumps is about 1.3 mJy beam^{-1}, we see significant polarized emission in MM2 but no emission in MM6. This is also the case at some of the highest contours in Stokes *I* in MM6.

To explore this apparent discrepancy further, we produced fractional polarization maps of the most polarized clumps (MM2 and MM3) and of those with the least amount of polarized emission (MM6 and MM7). The maps are shown in Figure 18. Although the MM8 clump is also not significantly polarized, we did not consider it here as it has the lower mass in our sample and the lack of polarized emission might therefore just be a sensitivity issue. The maps shown in Figure 18 were constructed by considering only the $3\sigma_{\rm poli}$ or greater polarized intensity (where $\sigma_{\rm poli} = \sqrt{\sigma_{\rm Q}^2 + \sigma_{\rm U}^2}$), which we used to create masks that were applied to the fractional polarization maps. Over the fractional polarization images, we superpose Stokes *I* emission from each clump by defining sensitivity contours of expected fractional polarization. To construct these contours,

we assumed a minimum polarized intensity $\min_{\rm poli} = 5\sigma_{\rm poli}$, which we later used to compute Stokes *I* levels of 10, 5, 3, 2, and 1% expected polarization.

The results suggests that, indeed, there are regions in MM6 and MM7, and also MM3, where we should have detected polarized emission but did not, as seen by checking the expected polarization contours in Figure 18. In MM6, the filament shows an unpolarized extension of about 6″ around core MM6-*A*, and in MM3, the whole shell appears to be unpolarized. For MM7 the map suggests that we should have been able to detect more polarized emission at the 15% level around core MM7-*A*, but we only detect emission at the 5 to 1% levels over the core itself. The origin of this lack of polarized emission cannot be completely explained from these data. However, there are some possibilities that we can explore. The clumps where the polarized emission is significant are also those with the least number of cores detected (or with a lower fragmentation degree). In MM2, MM3, and MM4 we detect about 8 cores in each clump, while for MM6, MM7, and MM8 we detect significantly more (13 cores in MM6, 21 in MM7, and 19 in MM8). It is clear that the fragmentation degree is higher in clumps where less polarization is detected. Although MM2 and MM3 are the most massive clumps in our sample, the MM4, MM6, and MM7 clumps are comparable in mass. This suggests that sensitivity to detected polarized emission is not an issue.

A plausible explanation might be related to grain alignment efficiency. In addition to the differences in the amount of polarized emission seen between the clumps, we see regions of strong and compact polarized dust emission in almost all clumps. Noteworthy is the case of core MM3-*F*, where the dust appears to be highly polarized up to 51%, although this region is at the edge of the lowest Stokes *I* contour used in our maps (see Figure 3). The current theoretical consensus suggests that grains are aligned by radiative torques produced by radiation fields (Lazarian & Hoang 2007; Lazarian & Thiem Hoang 2014). Thus, it is possible that we see the result of inner structures within these clumps, with preferred directions that allow efficient illumination of the dust in these regions. This type of preferential illumination might increase the efficiency in the alignment between the grains and the magnetic field. Now, it is harder to explain what we see in the regions where we do not see polarized emission just from a decrease in the grain alignment efficiency, especially considering the UC H II region, which is associated with the shell in the MM3 clump (see Section 3.1.2). If preferential illumination increases grain alignment efficiency, the radiation field from this star should have yielded detectable polarized emission from the MM3 shell. However, the shell is almost not polarized. In contrast, the MM4 UC H II region seems to be located within highly polarized emitting dust. Tang et al. (2009) mapped the UC H II region G5.89-0.39 with the SMA, where they found significant linear polarization coming from a dust ridge around the UC H II region. It is interesting to note that this ridge is located at one side with respect to the star, which migth also be the result of preferential illumination by the stellar radiation field. In our case, we see a small amount of polarized dust emission at the east side of the MM3 shell. The SMA data cannot be directly compared with ours, but it is clear that the effect of an UC H II region on the polarized dust emission is not understood and deserves more investigation.

Differences in clump fragmentation have also been observed in numerical simulations (Lee et al. 2017; Hennebelle 2018). These studies have suggested that magnetic fields play a significant role in the fragmentation of filamentary structures in star-forming regions. The simulations found that in nonmagnetized filaments the number of cores produced is in excess of what observations tell us. By introducing magnetic fields in the simulations, excessive fragmentation is suppressed and the obtained CMFs are closer to what is seen in the data. Our $B_{\rm pos} = 1.7$ mG estimate for MM7 is near the average value of the whole sample ($\langle B_{\rm pos}\rangle = 1.8$ mG), which makes it difficult to conclude unless the field outside the densest region is tangled along the line of sight, which will produce depolarization. If this is the case, the magnetic field might very well be a regulator of the number of protostellar cores formed and their initial masses. Hence, weak fields remain a possibility, and more observations are needed to understand these differences better.

5. Summary and Conclusions

In this work, we have presented high spatial resolution (∼0.01 pc) polarized dust emission ALMA observations of six of the most massive clumps from W43-Main, MM2, MM3, MM4, MM6, MM7, and MM8. The W43-MM1 results were presented in Paper I and were used in the virial analysis, see Section 4.1.3. The ALMA data revealed clumps with filamentary morphologies, where a total of 81 cores were extracted (96 when the MM1 cores are also considered). We also derived detailed magnetic field morphologies from these clumps by assuming magnetic grain alignment between the ambient magnetic field and the dust grains. From these morphologies, we were able to estimate the strength of the field and to evaluate the dynamical equilibrium of the cores detected here. Additionally, we obtained single-dish observations of the high-density molecular gas tracers HCN($J = 4 \rightarrow 3$) and HCO^+($J = 4 \rightarrow 3$), and archival ^{13}CO($J = 2 \rightarrow 1$) and $C^{18}O$ ($J = 2 \rightarrow 1$) observations to investigate the large-scale kinematics of these clumps. Detailed results are listed below.

1. We have found that the clumps mapped with ALMA can be divided into two populations of filaments. In one, the number of extracted cores is larger, suggesting increased fragmentation, and in the other, fragmentation is lower and the core distribution seems dominated by a single massive core. We identify the first population with the MM6, MM7, and MM8 clumps and the second with the MM2, MM3, and MM4 clumps. The MM2-*A* protostellar core is the most massive in our sample, with an estimated mass of 425.7 $M_\odot$. The core remains unresolved, but our calculations suggest that its evolution will result in a 30 $M_\odot$ O7 type star.
2. Two of our clumps, MM3 and MM4, are associated with UC H II regions. The MM3 clump shows two cavities, or a shell, which are not directly associated with any of the cores detected here. However, the G030.720-00.082 UC H II region is located within this shell, and it also seems to be associated with IRAC sources that are also located within the shell. It is therefore plausible that this shell is the result of the expanding shock and ionization fronts from a UC H II in MM3.
3. From the dust polarized emission, we derived the magnetic field morphologies from MM2, MM3, MM4,

and MM7. The field morphology from these clumps is quite ordered and spread out over significant portions of the filaments. Toward most of the massive cores, the field lines appear to have a projected radial pattern, suggesting that gravity dominates the field. However, over the filaments and away from the massive cores, we found that the field pattern appears to be along the filament with low EVPA dispersions, which suggests that magnetic tension is important.

4. We analyzed single-dish spectra from HCN($J = 4 \rightarrow 3$) and HCO^+($J = 4 \rightarrow 3$) to search for infalling motions. The blue asymmetry in the spectral profile from both lines toward MM2 and MM3 strongly suggests infalling. We quantified this asymmetry by computing the normalized velocity difference and fitting a simple infalling model to the line profile. We found consistent evidence supporting infall from scales of ~0.3 pc, obtaining infall rates of $\dot{M}_{\rm MM2} = 1.8 \times 10^{-2}\,M_\odot\,{\rm yr}^{-1}$ and $\dot{M}_{\rm MM3} = 6.3 \times 10^{-3}\,M_\odot\,{\rm yr}^{-1}$, which is high enough to overcome radiative feedback and form massive stars.
5. From the dust polarized emission we estimated the magnetic field strength onto the plane of sky, or $B_{\rm pos}$, using the original Davis–Chandrashekar–Fermi method with two additional derivations. We found average values for the field from 500 μG to a few mG (with a $\langle B_{\rm pos}\rangle = 1.8$ mG for the whole sample). The strongest value was estimated toward MM3-*F*, where we found $\langle B_{\rm pos}\rangle = 4.2$ mG. We used these estimates to analyze the dynamical equilibrium of the cores by calculating the total virial parameter, $\alpha_{\rm total}$, considering both turbulence and magnetic fields. We found 12 out of 17 bound cores and 5 unbound cores. We increased our statistics by assuming a $B_{\rm pos}$ value for the remaining cores. Here, we found that about half of our cores seem to be unbound, where these cores are also the least massive ones. Given that these cores are likely pressure-confined, we conclude that they should still be accreting to become self-gravitating at a later stage. Therefore, this strongly suggests different evolutionary timescales between the bound and unbound cores, and thus the star formation timescales in W43-Main might not be uniform.
6. We finally considered the difference in the distribution and strength of the polarized emission between the two populations of clumps in our sample. MM2, MM3, and MM4 are highly polarized, while MM6, MM7, and MM8 are not. We compared the fractional polarization maps with the Stokes *I* emission using "expected" contours where polarized emission should have been detected (with the exception of MM8, where the issue seems to be sensitivity). Thus, we found that in the MM6 and MM7 clumps the Stokes *I* emission was sufficient for succesful detections of polarized emission. However, and as previously said, these clumps are largely devoid of it. Moreover, the MM6, MM7, and MM8 clumps show significantly more fragmentation than the other clumps. Nonideal MHD mumerical simulations have suggested that the magnetic field has a direct impact on the degree of fragmentation seen in their simulated clumps. It is plausible that weaker magnetic fields in these clumps may explain this difference, but certainly, more data are needed to confirm this.

We acknowledge the useful comments made by the anonymous referee that certainly improved the representation of our results.

The National Radio Astronomy Observatory is a facility of the National Science Foundation operated under cooperative agreement by Associated Universities, Inc.

This paper makes use of the following ALMA data: ADS/JAO.ALMA#.2013.1.00725.S. ALMA is a partnership of ESO (representing its member states), NSF (USA) and NINS (Japan), together with NRC (Canada) and NSC and ASIAA (Taiwan), in cooperation with the Republic of Chile. The Joint ALMA Observatory is operated by ESO, AUI/NRAO and NAOJ.

J.M.G. acknowledges support from the Spanish AYA2017-84390-C2-2-R grant and the support from the Joint ALMA Observatory Visitor Program.

C.L.H.H. acknowledges the support of both the NAOJ Fellowship and JSPS KAKENHI grant 18K13586.

Z.Y.L. is supported in part by NASA grant 80NSSC18K1095 and NNX14B38G and NSF grant AST-1815784 and 1716259. S.P.L. thanks for the support of the Ministry of Science and Technology (MoST) of Taiwan through Grants NSC 98-2112-M-007-007-MY3, NSC 101-2119-M-007-004, and MoST 102-2119-M-007-004- MY3.

C.O. acknowledges the NRAO's Office of Diversity and Inclusion for its financial support of the undergraduate research experience program for Chilean students.

Software: CASA (v4.7 McMullin et al. 2007), NEWSTAR (Ikeda et al. 2001), APLpy (Robitaille & Bressert 2012).

Appendix A
The DCF Method

When perfect alignment between the ambient magnetic field and dust grains is assumed, the magnetic morphology onto the plane of sky can be inferred from the polarized dust emission by rotating the EVPA by 90° (for a review, see Lazarian & Hoang 2007). However, polarized emission from dust can only provide morphological information about the field, but not a direct measurement of its strength. Nevertheless, the field strength can be estimated from the field line pattern projected onto the plane of sky using the Davis, Chandrasekhar, & Fermi technique and its derivatives (hereafter DCF Davis 1951; Chandrasekhar & Fermi 1953). The usual DCF technique can be expressed as

$$B_{\rm pos} = 9.3\frac{\sqrt{n_{\rm H_2}}\,\Delta V}{\delta\phi}, \tag{9}$$

where $n_{\rm H_2}$ is the molecular hydrogen number density, ΔV represents the velocity dispersion in the gas, and $\delta\phi$ is the EVPA dispersion, which represents the perturbations in the magnetic field lines. A number of extensions, or derivatives, to the technique have been suggested to improve and account for the caveats of the original DCF technique. Heitsch et al. (2001) attempted to address the limitation of the small-angle approximation by replacing $\delta\phi$ by $\delta\tan(\phi)$, which is calculated locally, and by adding a geometric correction to avoid underestimating the field in the super-Alfvénic case. In contrast, Falceta-Gonçalves et al. (2008) assumed that the field perturbation is a global property, and they therefore replaced $\delta\phi$ by $\tan(\delta\phi) \sim \delta B/B_{\rm sky}$ in the denominator of Equation (9).

These two extensions can be written as

$$B_{\rm pos} = Q\frac{\sqrt{n_{\rm H_2}}\Delta V}{\tan\delta\phi} \quad (10)$$

$$B_{\rm pos} = Q\frac{\sqrt{n_{\rm H_2}}\Delta V}{\delta\tan\phi}(1+3(\delta\tan\phi)^2)^{1/4}, \quad (11)$$

where Q is a scaling factor. All the parameters used in the three calculation have large uncertainties, where ideally, these parameters should trace similar spatial scales. A main assumption behind the DCF method is that the field perturbations are produced by the nonthermal motions of the gas (turbulence). In fact, numerical simulations by Ostriker et al. (2001) showed that $\delta\phi < 25°$ values are able to reproduce the field strengths obtained from the simulations. However, the ALMA data show regions where $\delta\phi > 25°$ and where the field morphology also suggests that gravity might be behind the increased $\delta\phi$ values because the infalling gas might also pull the field along into the potential well of the core. Therefore, it is likely that the field strength is underestimated in these regions.

To trace the nonthermal motions of the gas, data from an optically thin and high-density molecular line tracer are required. At the clump scales, we have obtained HCN($J = 4 \rightarrow 3$) and HCO$^+$($J = 4 \rightarrow 3$) data for MM2 and MM3, but the H^{13}CO$^+$($J = 3 \rightarrow 2$) observations from Motte et al. (2003) are also available in the literature. However, the HCN($J = 4 \rightarrow 3$) and HCO$^+$($J = 4 \rightarrow 3$) has been shown to be optically thick (see Section 3.3) and therefore cannot be used reliably to trace the gas turbulent motions. The H^{13}CO$^+$($J = 3 \rightarrow 2$) emission, however, is likely optically thin for some of our clumps. The resolution of these data is $\sim$26″, or $\sim$0.7 pc, which as a first approximation can be used to derive ΔV at the clump scale. Nonetheless, we can estimate ΔV at smaller scales if we assume a Kolmogorov type turbulent power spectrum. A usual expression for a Kolmogorov type turbulence power spectrum is given by $\sigma_{\rm v}^2 = bL^n$. Here, $\sigma_{\rm v}$ corresponds to the velocity dispersion of a molecular line, as expected from the turbulence energy cascade at length scale L. To obtain the power law, we require to know b, a scaling constant, and n the power-law exponent. Li & Houde (2008) derived $n = 0.36$ from their M17 emission, which is a well-studied high-mass star-forming region. Unfortunately, we do not have sufficient single-dish data to fit the power law and derive the parameters ourselves. Nevertheless, the values derived from M17 by Li & Houde (2008) are in concordance with what is seen in other high-mass star-forming regions (Tang et al. 2018) and is an acceptable representation for the nonthermal motions in W43-Main. In fact, molecular line observations of C^{18}O(2–1) at similar length scales from G28.34 reveal velocity dispersions $\sigma_{\rm C^{18}O} \sim 0.7$ km s^{-1} (Zhang et al. 2015). These values are similar to our estimate, although C^{18}O(2–1) traces a more diffuse environment than H^{13}CO$^+$(3-2). The C^{18}O(2–1) line width can be enlarged by adding turbulence to the gas by outflows and infall, which is indeed true for W43-Main clumps, where evidence for infalling motions and outflows have been detected. The H^{13}CO$^+$ ($3 \rightarrow 2$) data show a large spread in the line widths from 3.6 to 6.3 km s^{-1} for MM4 and MM8, respectively, with values in between for the other clumps (see Table 2 in Motte et al. 2003). Starting from clump scales, we can obtain the b values for each clump, as $b = \sigma^2_{\rm H^{13}CO^+}/L^n$. Later the estimation for the velocity dispersion, $\sigma_{\rm v}$, can be obtained by using the relevant angular scale, where the line width, ΔV, is given by multiplying by the FWHM value, or $\Delta V = 2\sqrt{2\log 2}\,\sigma_{\rm v}$. The derived values of b are listed in Table 6.

The dispersion of the EVPA, $\delta\phi$, requires closer attention. We use the standard deviation of the EVPA values from the polarization map as our estimator of the dispersion. When we assume that the distribution of EVPA values is Gaussian, 10 beam-independent points give us a dispersion value within 15% from the true dispersion. Here we defined an independent point as a Nyquist-sampled cell in the map. This criterion gives a minimum threshold to use the polarization data in the $B_{\rm pos}$ estimation. However, the exquisite sensitivity of ALMA gives us a much larger number of independent points, which decreases the uncertainty significantly. We use this threshold to establish a criterion to define regions where the field shows an apparent coherence. We do this by requiring continuity in the field lines, or a smooth variation in EVPA, from subregions where we have 10 independent points, the minimum threshold needed to estimate $\delta\phi$. Therefore, a region where we estimate $B_{\rm pos}$ is composed of continuous EVPA measurements. We justify this as the underlying assumptions in the DCF method are that the field in-frozen in the fluid and the perturbations in the Alfvén waves occur at small scales. Therefore we cannot consider the dispersion in the field from a whole filament unless its dispersion is small. Based on these considerations, the clumps where the polarized emission is sufficient to satisfy our constraints are MM2, MM3, MM4 from population 2 and only MM7 from population 1. As previously identified, the remaining clumps from population 1 (MM6 and MM8) have well-defined regions with polarized emission, but not sufficient independent points. We discuss this in Section 4.2. Thus, we divided the polarized emission in regions (as done in Paper I) where the field appears to be continuous and calculated the required parameters for the region length scale (see Section 3.2 for details).

Finally, the number density is estimated by computing the column density for the region and assuming spherical geometry. In this way, we accounted for perturbation by the ambient gas in the field lines, which provides consistency in the calculation. However, this field strength is not necessarily representative of core field strengths as $B \sim \sqrt{\rho}$ (Ciolek 1995) or $B \sim \rho^{2/3}$ (Mestel 1966). In either case, the total field strength might be higher than the values we estimated here.

Appendix B
Infalling Methods

The ratio between the difference in the velocities, associated with the peak emission between the optically thick and the optically thin lines, with respect to the line width from the optically thin emission is known as the normalized line velocity difference (Mardones et al. 1997),

$$\Delta V_{\rm be} = \frac{V^{\rm max}_{\rm thick} - V^{\rm max}_{\rm thin}}{\Delta V_{\rm thin}}, \quad (12)$$

where $V^{\rm max}_{\rm thick}$ is the velocity from the peak emission of the optically think line, $V^{\rm max}_{\rm thin}$ is the velocity from the peak emission of the optically thin line, and $\Delta V_{\rm thin}$ is the line width from the optically thin molecular tracer. A negative $\Delta V_{\rm be}$ indicates blueshifted gas velocities, which is suggestive of infalling motions.

The normalized velocity difference is not sufficient to characterize infalling motions. A more detailed model is needed

Table 3
Physical Parameters for Each of the Cores

Clump	Core	R.A. (J2000)	Decl. (J2000)	Peak (mJy beam^{-1})	Flux (mJy)	Major[a] (arcsec)	Minor[a] (arcsec)	P.A. (deg)	n[b] (10^7 cm^{-3})	Mass ($M_\odot$)	Size[c] (mpc)	λ_J (mpc)	M_J ($M_\odot$)	M_T ($M_\odot$)
	A	18:47:36.79	−02:00:54.15	354.1 ± 17.8	879.8	0.79	0.63	149.80	283.7	425.7	18.82	0.60	0.02	6.03
	B	18:47:36.69	−02:00:47.63	27.4 ± 2.1	79.7	0.95	0.64	25.57	19.3	38.6	20.72	2.32	0.07	6.64
	C	18:47:36.28	−02:00:50.69	17.7 ± 1.2	32.8	0.57	0.47	20.16	26.4	15.9	13.87	1.98	0.06	4.44
	D	18:47:36.66	−02:00:53.22	21.4 ± 4.2	87.1	1.21	0.90	77.42	8.7	42.1	27.80	3.44	0.11	8.90
MM2	E	18:47:36.15	−02:00:47.76	12.9 ± 0.7	17.4	0.44	0.17	43.31	94.5	8.4	7.34	1.05	0.03	2.35
	F	18:47:36.82	−02:00:50.30	13.6 ± 1.4	46.4	0.99	0.82	3.02	7.2	22.4	24.03	3.79	0.12	7.70
	G	18:47:36.84	−02:01:2.60	14.0 ± 1.0	28.2	0.77	0.40	143.18	19.1	13.7	14.71	2.33	0.07	4.71
	H	18:47:36.14	−02:00:46.54	6.1 ± 0.6	9.7	0.57	0.33	132.75	13.6	4.7	11.54	2.76	0.09	3.70
	I	18:47:35.99	−02:00:49.75	6.0 ± 0.7	43.3	1.90	1.12	55.18	1.6	20.9	38.98	8.11	0.25	12.49
	J	18:47:36.74	−02:00:46.64	4.3 ± 1.7	9.2	0.91	0.37	64.82	5.3	4.5	15.53	4.42	0.14	4.97
	A	18:47:41.71	−02:00:28.51	76.1 ± 5.5	149.9	0.72	0.49	98.23	67.4	59.4	15.77	1.34	0.05	5.19
	B	18:47:41.73	−02:00:27.29	39.2 ± 3.7	84.8	0.94	0.41	120.45	32.9	33.6	16.57	1.92	0.07	5.45
	C	18:47:41.62	−02:00:25.25	20.8 ± 1.7	51.7	0.78	0.66	125.23	12.9	20.5	19.20	3.07	0.11	6.32
MM3	D	18:47:41.60	−02:00:28.29	12.6 ± 1.5	35.0	1.15	0.55	93.33	6.4	13.9	21.31	4.36	0.16	7.01
	E	18:47:41.81	−02:00:29.21	18.4 ± 2.4	104.8	1.96	0.85	107.35	4.5	41.6	34.47	5.19	0.19	11.34
	F	18:47:41.99	−02:00:28.04	8.7 ± 0.8	16.6	0.69	0.48	100.28	8.3	6.6	15.26	3.83	0.14	5.02
	G	18:47:40.97	−02:00:20.67	9.9 ± 0.7	19.6	0.63	0.54	86.17	9.2	7.8	15.55	3.64	0.13	5.12
	H	18:47:41.86	−02:00:27.83	9.1 ± 0.2	58.8	1.79	1.09	82.19	2.0	23.3	37.27	7.78	0.28	12.27
	A	18:47:38.44	−01:57:42.62	22.6 ± 3.1	159.6	2.13	1.18	74.89	3.6	60.6	42.16	5.92	0.22	8.59
	B	18:47:38.70	−01:57:45.12	11.2 ± 0.9	53.0	1.31	1.16	127.05	2.5	20.1	32.89	7.07	0.27	6.70
	C	18:47:38.10	−01:57:50.61	7.0 ± 0.6	17.4	1.13	0.52	88.89	3.4	6.6	20.53	6.10	0.23	4.18
MM4	D	18:47:37.75	−01:57:51.40	7.6 ± 0.3	21.1	1.15	0.59	57.31	3.3	8.0	22.03	6.14	0.23	4.49
	E	18:47:38.25	−01:57:40.73	6.7 ± 0.4	22.7	1.55	0.60	73.94	2.3	8.6	25.66	7.45	0.28	5.23
	F	18:47:38.56	−01:57:43.59	12.2 ± 0.1	64.0	1.64	1.07	106.15	2.5	24.3	35.28	7.15	0.27	7.18
	G	18:47:37.97	−01:57:50.35	5.4 ± 0.1	41.3	2.20	1.19	32.91	0.9	15.7	43.15	12.04	0.45	8.79
	H	18:47:38.86	−01:57:41.97	3.6 ± 0.0	22.2	1.55	1.40	84.38	0.6	8.4	39.18	14.20	0.54	7.98
	A	18:47:35.80	−01:55:10.86	20.5 ± 1.5	52.0	0.87	0.70	78.28	11.1	22.7	20.89	3.19	0.11	5.99
	B	18:47:35.58	−01:55:18.58	9.9 ± 1.4	23.0	0.80	0.62	27.08	6.8	10.0	18.67	4.05	0.14	5.35
	C	18:47:36.52	−01:55:19.69	11.7 ± 0.2	13.3	0.24	0.20	15.77	129.2	5.8	5.84	0.93	0.03	1.67
	D	18:47:35.53	−01:55:19.51	5.3 ± 0.1	9.7	0.63	0.48	25.24	5.9	4.2	14.74	4.36	0.15	4.22
	E	18:47:35.55	−01:55:17.07	4.0 ± 0.9	19.0	1.67	0.89	116.92	1.1	8.3	32.48	10.21	0.34	9.31
MM6	F	18:47:36.01	−01:55:20.53	1.8 ± 0.2	3.1	0.73	0.36	75.65	2.4	1.4	13.65	6.88	0.23	3.91
	G	18:47:35.33	−01:55:19.93	3.5 ± 0.4	25.9	2.20	1.16	73.59	0.6	11.3	42.60	13.15	0.44	12.21
	H	18:47:35.85	−01:55:15.44	2.9 ± 0.3	16.5	1.57	1.16	128.28	0.7	7.2	36.03	12.80	0.43	10.33
	I	18:47:35.34	−01:55:21.99	2.2 ± 0.0	7.7	1.31	0.67	140.76	1.0	3.4	25.02	10.85	0.37	7.17
	J	18:47:35.41	−01:55:22.82	2.2 ± 0.1	8.4	1.19	0.93	151.89	0.7	3.7	28.06	12.35	0.42	8.04
	K	18:47:36.18	−01:55:20.52	1.6 ± 0.2	4.4	1.15	0.59	81.71	0.8	1.9	22.02	11.89	0.40	6.31
	L	18:47:35.78	−01:55:13.88	6.5 ± 0.1	62.2	2.43	1.39	58.72	1.0	27.1	48.91	10.44	0.35	14.02
	M	18:47:35.66	−01:55:15.74	3.1 ± 0.0	19.5	1.79	1.18	120.81	0.6	8.5	38.77	13.16	0.44	11.11
	A	18:47:39.65	−01:58:32.47	15.4 ± 0.8	26.9	0.57	0.49	131.27	15.6	11.7	14.05	2.23	0.06	3.91
	B	18:47:39.11	−01:58:39.98	12.3 ± 0.8	27.1	0.79	0.53	158.24	8.5	11.8	17.27	3.03	0.08	4.81
	C	18:47:39.61	−01:58:33.67	7.7 ± 1.2	22.9	1.14	0.67	114.18	3.0	10.0	23.18	5.12	0.14	6.46
	D	18:47:39.65	−01:58:35.04	5.8 ± 0.3	11.7	0.68	0.52	3.36	4.6	5.1	15.94	4.09	0.11	4.44
	E	18:47:39.80	−01:58:23.00	5.8 ± 0.1	7.2	0.33	0.27	39.47	23.1	3.1	7.95	1.83	0.05	2.22
	F	18:47:40.18	−01:58:38.78	5.7 ± 0.3	11.9	0.68	0.59	127.28	3.9	5.2	17.00	4.47	0.13	4.74

Table 3
(Continued)

Clump	Core	R.A. (J2000)	Decl. (J2000)	Peak (mJy beam^{-1})	Flux (mJy)	Major[a] (arcsec)	Minor[a] (arcsec)	P.A. (deg)	n[b] (10^7 cm^{-3})	Mass ($M_\odot$)	Size[c] (mpc)	λ_J (mpc)	M_J ($M_\odot$)	M_T ($M_\odot$)
	G	18:47:40.19	−01:58:30.95	3.3 ± 0.2	4.0	0.39	0.20	80.71	15.2	1.7	7.50	2.26	0.06	2.09
	H	18:47:39.60	−01:58:28.16	3.8 ± 0.3	17.0	1.35	1.00	125.13	0.9	7.4	31.07	9.21	0.26	8.65
	I	18:47:38.50	−01:58:21.17	10.7 ± 0.9	21.7	0.75	0.54	87.22	7.3	9.5	16.85	3.26	0.09	4.69
	J	18:47:39.47	−01:58:30.78	2.6 ± 0.2	8.3	1.15	0.65	15.99	1.1	3.6	22.95	8.39	0.24	6.39
MM7	K	18:47:40.20	−01:58:40.30	5.6 ± 0.6	27.7	1.55	0.90	2.00	1.4	12.1	31.53	7.39	0.21	8.78
	L	18:47:39.63	−01:58:29.85	2.9 ± 0.2	13.1	1.56	0.80	157.22	0.8	5.7	29.75	9.86	0.28	8.29
	M	18:47:40.23	−01:58:36.58	2.7 ± 0.2	6.5	0.95	0.57	93.20	1.4	2.9	19.53	7.40	0.21	5.44
	N	18:47:39.89	−01:58:33.39	1.9 ± 0.1	4.9	1.29	0.36	59.49	1.3	2.1	18.10	7.64	0.21	5.04
	O	18:47:40.17	−01:58:31.81	2.1 ± 0.4	7.2	1.06	0.81	165.71	0.8	3.1	24.76	10.10	0.28	6.90
	P	18:47:39.44	−01:58:31.73	2.4 ± 0.1	11.7	1.76	0.83	63.42	0.6	5.1	32.11	11.66	0.33	8.94
	Q	18:47:39.09	−01:58:42.12	2.6 ± 0.3	10.8	1.65	0.56	6.57	1.0	4.7	25.53	8.61	0.24	7.11
	R	18:47:38.89	−01:58:20.15	3.3 ± 0.2	7.8	0.84	0.60	141.21	1.9	3.4	18.95	6.47	0.18	5.28
	S	18:47:38.90	−01:58:20.84	2.3 ± 0.1	8.5	1.20	0.86	132.71	0.7	3.7	27.02	10.61	0.30	7.53
	T	18:47:39.37	−01:58:23.73	2.4 ± 0.1	8.3	1.13	0.86	110.48	0.7	3.6	26.29	10.29	0.29	7.32
	U	18:47:39.43	−01:58:24.36	2.5 ± 0.0	15.7	2.06	1.01	91.72	0.4	6.8	38.33	13.16	0.37	10.67
	V	18:47:39.57	−01:58:25.41	2.5 ± 0.1	9.1	1.38	0.62	161.16	1.0	4.0	24.62	8.88	0.25	6.86
	A	18:47:36.52	−01:55:19.64	11.8 ± 0.2	13.3	0.22	0.20	77.40	149.3	5.8	5.57	0.87	0.03	1.60
	B	18:47:36.58	−01:55:33.17	14.7 ± 0.6	27.4	0.57	0.50	14.39	18.6	11.9	14.19	2.46	0.08	4.07
	C	18:47:36.49	−01:55:33.76	8.7 ± 0.8	18.3	0.86	0.42	68.01	8.6	8.0	16.03	3.61	0.12	4.60
	D	18:47:36.39	−01:55:35.19	14.9 ± 0.9	54.6	1.28	0.61	11.19	8.1	23.8	23.54	3.72	0.13	6.75
	E	18:47:36.60	−01:55:32.39	8.4 ± 0.4	34.8	1.54	0.55	6.58	4.6	15.2	24.51	4.95	0.17	7.02
	F	18:47:36.64	−01:55:35.14	4.5 ± 0.4	11.4	0.87	0.55	170.32	3.6	5.0	18.37	5.61	0.19	5.27
	G	18:47:36.44	−01:55:28.27	2.7 ± 0.3	4.6	0.57	0.40	50.33	4.2	2.0	12.78	5.15	0.17	3.66
	H	18:47:37.19	−01:55:26.31	1.4 ± 0.2	2.0	0.52	0.19	40.05	6.5	0.9	8.41	4.15	0.14	2.41
	I	18:47:37.25	−01:55:28.58	1.6 ± 0.1	4.9	0.98	0.64	12.62	1.0	2.1	21.15	10.59	0.36	6.06
MM8	J	18:47:36.74	−01:55:32.74	2.1 ± 0.2	8.6	1.56	0.67	81.53	0.8	3.7	27.37	11.77	0.40	7.85
	K	18:47:37.70	−01:55:24.23	1.3 ± 0.3	4.0	1.52	0.39	71.72	0.9	1.7	20.59	11.28	0.38	5.90
	L	18:47:35.90	−01:55:35.12	3.7 ± 0.3	8.8	0.71	0.67	49.76	2.8	3.8	18.31	6.36	0.21	5.25
	M	18:47:37.25	−01:55:27.56	1.5 ± 0.0	7.1	1.53	0.78	24.31	0.6	3.1	29.19	14.26	0.48	8.37
	N	18:47:37.42	−01:55:22.25	1.3 ± 0.1	8.0	1.52	1.17	20.39	0.3	3.5	35.68	18.15	0.61	10.23
	O	18:47:37.36	−01:55:24.55	1.2 ± 0.1	4.9	1.28	0.91	98.82	0.4	2.1	28.71	16.72	0.56	8.23
	P	18:47:36.17	−01:55:20.38	1.6 ± 0.2	6.4	1.36	0.77	101.12	0.6	2.8	27.23	13.53	0.46	7.80
	Q	18:47:36.01	−01:55:20.44	1.9 ± 0.3	5.9	1.24	0.62	87.22	0.9	2.6	23.34	11.12	0.38	6.69
	R	18:47:36.17	−01:55:30.99	1.1 ± 0.2	1.8	0.63	0.40	126.53	1.5	0.8	13.32	8.60	0.29	3.82
	S	18:47:37.26	−01:55:23.46	1.0 ± 0.1	6.5	1.61	1.16	153.02	0.3	2.8	36.43	20.76	0.70	10.44
	T	18:47:36.93	−01:55:28.86	0.9 ± 0.0	4.3	1.29	1.07	117.06	0.3	1.9	31.30	20.24	0.68	8.97

Notes. Additionally, we show here the Jeans length (λ_J) and mass (M_J), as well as the kinetic mass ($M_{\rm kin}$) values for each core.

[a] Deconvolved major and minor axes are obtained from the Gaussian fitting procedure.

[b] Volume number densities were calculated assuming spherical geometry.

[c] The fragment size is calculated as $d = 5500{*}\sqrt{b_{\rm maj} \times b_{\rm min}}$ [pc].

Table 4
Polarization Parameters and the Magnetic Field Estimates on the Plane of Sky Using Three Versions of the DCF Method

Clump	Core	Region	N[a] (10^{24} cm^{-2})	$\langle\phi\rangle$[b] (°)	$\delta\phi$[b] (°)	$F_{\rm min}$[b] (%)	$F_{\rm max}$[b] (%)	$\langle F\rangle$[b] (%)	B_1[c] (mG)	B_2[d] (mG)	B_3[e] (mG)	λ_{B_1}[f]	λ_{B_2}[g]	λ_{B_3}[h]
	A	1	47.5	−23.9	39.6	0.02	7.8	2.5	>2.2	>3.2	>0.6	<53.5	<37.8	<208.1
	B	3	3.6	7.9	43.6	0.07	26.3	5.1	1.0	1.4	0.5	8.6	6.4	18.9
MM2	C	4	3.3	26.1	40.2	0.45	7.0	3.5	0.8	1.1	0.2	10.8	7.7	47.4
	D	1	2.2	−23.9	39.6	0.02	7.8	2.5	>2.2	>3.2	>0.6	<2.4	<1.7	<9.4
	F	2	1.5	2.2	66.1	0.19	14.2	5.1	0.5	0.5	0.1	7.4	8.6	36.4
	J	3	0.7	7.9	43.6	0.07	26.3	5.1	1.0	1.4	0.5	1.8	1.3	3.9
	A	3	9.5	−8.5	42.8	0.01	8.3	2.4	>1.0	>1.4	>0.1	<23.3	<17.0	<292.0
	B	3	4.8	−8.5	42.8	0.01	8.3	2.4	>1.0	>1.4	>0.1	<12.0	<8.7	<149.7
MM3	C	4	2.2	50.1	33.2	0.06	14.3	5.0	1.3	2.0	0.4	4.2	2.8	12.4
	D	3	1.2	−8.5	42.8	0.01	8.3	2.4	>1.0	>1.4	>0.1	<3.0	<2.2	<37.4
	E	2	1.4	−24.9	15.6	0.09	5.2	2.8	4.0	6.5	5.9	0.9	0.5	0.6
	F	1	1.1	−38.2	10.3	0.24	51.6	23.4	3.3	5.6	3.7	0.9	0.5	0.8
MM4	A	1	1.3	−56.7	22.1	0.11	6.1	2.2	1.4	2.3	0.1	2.4	1.5	32.6
	F	1	0.8	−56.7	22.1	0.11	6.1	2.2	1.4	2.3	0.1	1.3	0.8	18.7
MM7	H	1	0.3	67.8	10.8	0.46	19.2	11.0	1.7	2.9	0.6	0.4	0.3	1.4
	K	1	0.5	67.8	10.8	0.46	19.2	11.0	1.7	2.9	0.6	0.7	0.4	2.2

Notes. The polarization parameters are calculated from the 3σ data. We also show the ratio of mass to magnetic flux (λ_B) for each of the cores where we have estimates of field strength. For the MM2 and MM3 clumps, some of our estimates for $B_{\rm pos}$ are lower limits, which we indicate using the >sign. In the same way, these lower limits give upper limits for λ_B, which we indicate using the <sign.
[a] The column density displayed here corresponds to the core column density indicated by its letter, not the region used to extract $\delta\phi$.
[b] Here $\langle\phi\rangle$ is the average EVPA, $\delta\phi$ is the EVPA dispersion (calculated using circular statistics), $F_{\rm min}$ is the minumum fractional polarization, $F_{\rm max}$ is the maximun fractional polarization, and $\langle F\rangle$ is the average fractional polarization value. All values are computed for the pixels in the region indicated in Column 2.
[c] Estimates of the magnetic field in the plane of sky obtained with the original CF method (see Equation (9) in the text).
[d] Estimates of the magnetic field in the plane of sky obtained using the corrections implemented by Falceta-Gonçalves et al. (2008; Equation (9)).
[e] Estimates of the magnetic field in the plane of sky obtained using the corrections implemented by Heitsch et al. (2001; Equation (12)).
[f] Estimate of the ratio of the mass to magnetic flux using the field strength estimate B_1.
[g] Estimate of the ratio of the mass to magnetic flux using the field strength estimate B_2.
[h] Estimate of the ratio of the mass to magnetic flux using the field strength estimate B_3.

Table 5
Results from the Infall Model Fit

Clump	Line	ϕ	τ_0	$J(T_c)$ (K)	$J(T_f)$ (K)	$J(T_r)$ (K)	$v_{\rm lsr}$ (km s^{-1})	σ (km s^{-1})	v_f (km s^{-1})	v_r (km s^{-1})
MM2	HCN	0.080	0.0	12.7	70.2	104.4	90.8	1.4	2.9	1.3
MM2	HCN	0.080	2.2	12.7	1.9	1.8	90.8	1.7	2.8	0.1
MM2	HCO^+	0.080	1.0	12.6	0.0	4.4	90.8	2.2	0.4	−0.1
MM2	HCO^+	0.080	1.0	12.6	0.0	4.4	90.8	2.2	0.4	−0.0
MM3	HCN	0.080	0.8	12.7	2.5	2.3	93.5	1.5	3.3	1.9
MM3	HCN	0.080	0.0	12.7	110.0	193.0	93.5	2.0	3.5	1.8
MM3	HCO^+	0.080	1.4	12.6	0.0	7.6	93.5	1.8	0.8	−0.5
MM3	HCO^+	0.080	1.3	12.6	0.0	7.5	93.5	1.9	0.9	−0.6

to derive the flow parameters, especially the mass infall rate. Such a model was developed by Myers et al. (1996) and Di Francesco et al. (2001), where the clump is approximated by two infalling gas layers, a front and a rear layer, with a central source simulating the prestellar core. Thus, the observed brightness temperature is quantified by the following equation, where the subscripts "f," "r," "C," and "cmb" stand for the front layer, the rear layer, the central source, and the cosmic background emission. The model is described by the following equation:

$$\Delta T_{\rm B} = (J_{\rm f} - J_{\rm C})[1 - e^{-\tau_{\rm f}}] + (1 - \Phi)(J_{\rm r} - J_{\rm cmb})[1 - e^{-(\tau_{\rm r}+\tau_{\rm f})}]. \quad (13)$$

The main terms in this equation are the Planck excitation temperature, given by $J_{\rm i} = T_0/[\exp(T_0/T_{\rm i}) - 1]$ with $T_0 = h\nu/k$, and $T_{\rm i}$, corresponding to either $T_{\rm f}$, $T_{\rm r}$, $T_{\rm c}$, or $T_{\rm cmb}$. Also, $J_{\rm C} = \Phi\ {\rm J_c} + (1 - \Phi)J_{\rm r}$, where Φ is the beam filling factor of the continuum source, which due to the large beam size of the ASTE telescope is assumed to be 0. The $\tau_{\rm i}$ expressions correspond to the optical depths, which we assumed to be Gaussian. Thus and following Myers et al. (1996), the front and rear optical depths are given by

$$\tau_{\rm f} = \tau_0 \exp\left[\frac{-(v - v_{\rm f} - v_{\rm lsr})^2}{2\sigma^2}\right] \quad (14)$$

$$\tau_{\rm r} = \tau_0 \exp\left[\frac{-(v + v_{\rm r} - v_{\rm lsr})^2}{2\sigma^2}\right], \quad (15)$$

Table 6
Velocity Dispersion for Each Clump

Clump	b (km^2 s^{-2} arcsec^{-n})	$\sigma_{\rm CSO}$ (km s^{-1})	$\sigma_{\rm B}$ (km s^{-1})	$\sigma_{\rm core}$ (km s^{-1})
MM2	0.54	1.78	0.99	0.74
MM3	0.57	1.87	1.01	0.76
MM4	0.35	1.14	0.79	0.59
MM6	0.49	1.61	⋯	0.7
MM7	0.48	1.57	0.93	0.69
MM8	0.49	1.61	⋯	0.7

Note. The values for σ are derived assuming the turbulent power spectrum $\sigma^2 = bL^n$ as indicated in the text. Here $\sigma_{\rm CSO}$ gives the velocity dispersion calculated from the $H^{13}CO^+(3 \rightarrow 2)$ taken from Table 2 in Motte et al. (2003; see text for a discussion on MM4, MM6, and MM8.), $\sigma_{\rm B}$ gives the values for the length scales traced by the magnetic field region, and $\sigma_{\rm core}$ is the velocity dispersion for the core scales, or $1''$.

where τ_0 is the peak optical depth for both the front and the rear layers, $v_{\rm f}$ and $v_{\rm r}$ are the infalling velocities for both slabs, and σ is the velocity dispersion.

ORCID iDs

Paulo C. Cortes https://orcid.org/0000-0002-3583-780X
Charles L. H. Hull https://orcid.org/0000-0002-8975-7573
Josep M. Girart https://orcid.org/0000-0002-3829-5591
Shih-Ping Lai https://orcid.org/0000-0001-5522-486X

References

Alves, J., Lombardi, M., & Lada, C. J. 2007, A&A, 462, L17
André, P., Revéret, V., Könyves, V., et al. 2016, A&A, 592, A54
Arzoumanian, D., André, P., Didelon, P., et al. 2011, A&A, 529, L6
Bally, J., Anderson, L. D., Battersby, C., et al. 2010, A&A, 518, L90
Balser, D. S., Goss, W. M., & De Pree, C. G. 2001, AJ, 121, 371
Bastian, N., Covey, K. R., & Meyer, M. R. 2010, ARA&A, 48, 339
Bertoldi, F., & McKee, C. F. 1992, ApJ, 395, 140
Blum, R. D., Damineli, A., & Conti, P. S. 1999, AJ, 117, 1392
Carlhoff, P., Nguyen Luong, Q., Schilke, P., et al. 2013, A&A, 560, A24
Cesaroni, R., Palagi, F., Felli, M., et al. 1988, A&AS, 76, 445
Chandrasekhar, S., & Fermi, E. 1953, ApJ, 118, 113
Ciolek, G. E. 1995, in ASP Conf. Ser. 80: The Physics of the Interstellar Medium and Intergalactic Medium, ed. A. Ferrara et al. (San Francisco, CA: ASP), 174
Cortes, P., & Crutcher, R. M. 2006, ApJ, 639, 965
Cortes, P. C., Girart, J. M., Hull, C. L. H., et al. 2016, ApJL, 825, L15
Cortes, P. C., Parra, R., Cortes, J. R., & Hardy, E. 2010, A&A, 519, A35
Crutcher, R. M. 2012, ARA&A, 50, 29
Crutcher, R. M., Nutter, D. J., Ward-Thompson, D., & Kirk, J. M. 2004, ApJ, 600, 279
Cyganowski, C. J., Brogan, C. L., Hunter, T. R., et al. 2017, MNRAS, 468, 3694
Davis, L. 1951, PhRv, 81, 890
Di Francesco, J., Myers, P. C., Wilner, D. J., Ohashi, N., & Mardones, D. 2001, ApJ, 562, 770
Falceta-Gonçalves, D., Lazarian, A., & Kowal, G. 2008, ApJ, 679, 537
Fazal, F. M., Sridharan, T. K., Qiu, K., et al. 2008, ApJL, 688, L41
Fissel, L. M., Ade, P. A. R., Angilè, F. E., et al. 2016, ApJ, 824, 134
Frau, P., Girart, J. M., Zhang, Q., & Rao, R. 2014, A&A, 567, A116
Girart, J. M., Beltrán, M. T., Zhang, Q., Rao, R., & Estalella, R. 2009, Sci, 324, 1408
Hamakerr, J. P., & Bregman, J. D. 1996, A&AS, 117, 149
Heap, S. R., Lanz, T., & Hubeny, I. 2006, ApJ, 638, 409
Heitsch, F., Zweibel, E. G., Mac Low, M.-M., Li, P., & Norman, M. L. 2001, ApJ, 561, 800
Hennebelle, P. 2018, A&A, 611, A24
Herpin, F., Marseille, M., Wakelam, V., Bontemps, S., & Lis, D. C. 2009, A&A, 504, 853
Hull, C. L. H., Girart, J. M., Kristensen, L. E., et al. 2016, ApJL, 823, L27
Hull, C. L. H., Plambeck, R. L., Kwon, W., et al. 2014, ApJS, 213, 13
Hull, C. L. H., & Zhang, Q. 2019, FrASS, 6, 3
Hunter, J. D. 2007, CSE, 9, 90
Ikeda, M., Nishiyama, K., Ohishi, M., & Tatematsu, K. 2001, in ASP Conf. Ser. 238, Astronomical Data Analysis Software and Systems X, ed. J. Harnden et al. (San Francisco, CA: ASP), 522
Juárez, C., Girart, J. M., Zamora-Avilés, M., et al. 2017, ApJ, 844, 44
Kohno, K. 2005, in ASP Conf. Ser. 344, The Cool Universe: Observing Cosmic Dawn, ed. C. Lidman & D. Alloin (San Francisco, CA: ASP), 242
Lada, C. J., & Lada, E. A. 2003, ARA&A, 41, 57
Larson, R. B. 2003, RPPh, 66, 1651
Lazarian, A., & Hoang, T. 2007, MNRAS, 378, 910
Lazarian, A., & Thiem Hoang, C. 2014, in COSPAR Meeting 40, XL COSPAR Scientific Assembly F3.2–4–14
Lee, Y.-N., Hennebelle, P., & Chabrier, G. 2017, ApJ, 847, 114
Leung, C. M., & Brown, R. L. 1977, ApJL, 214, L73
Li, H.-b., & Houde, M. 2008, ApJ, 677, 1151
Liszt, H. S. 1995, AJ, 109, 1204
Louvet, F., Motte, F., Hennebelle, P., et al. 2014, A&A, 570, A15
Lu, X., Zhang, Q., Liu, H. B., et al. 2018, ApJ, 855, 9
MacLaren, I., Richardson, K. M., & Wolfendale, A. W. 1988, ApJ, 333, 821
Mardones, D., Myers, P. C., Tafalla, M., et al. 1997, ApJ, 489, 719
Maury, A. J., Girart, J. M., Zhang, Q., et al. 2018, MNRAS, 477, 2760
McKee, C. F., & Tan, J. C. 2003, ApJ, 585, 850
McMullin, J. P., Waters, B., Schiebel, D., Young, W., & Golap, K. 2007, in ASP Conf. Ser. 376, Astronomical Data Analysis Software and Systems XVI, ed. R. A. Shaw, F. Hill, & D. J. Bell (San Francisco, CA: ASP), 127
Men'shchikov, A., André, P., Didelon, P., et al. 2012, A&A, 542, A81
Mestel, L. 1966, MNRAS, 133, 265
Mooney, T., Sievers, A., Mezger, P. G., et al. 1995, A&A, 299, 869
Motte, F., Nony, T., Louvet, F., et al. 2018, NatAs, 2, 478
Motte, F., Schilke, P., & Lis, D. C. 2003, ApJ, 582, 277
Mouschovias, T. C. 1987, in NATO ASIC Proc. 210: Physical Processes in Interstellar Clouds, 491
Myers, P. C., Mardones, D., Tafalla, M., Williams, J. P., & Wilner, D. J. 1996, ApJL, 465, L133
Nakano, T., & Nakamura, T. 1978, PASJ, 30, 671
Nguyen-Lu'o'ng, Q., Motte, F., Carlhoff, P., et al. 2013, ApJ, 775, 88
Nguyen-Luong, Q., Anderson, L. D., Motte, F., et al. 2017, ApJL, 844, L25
Ossenkopf, V., & Henning, T. 1994, A&A, 291, 943
Ostriker, E. C., Stone, J. M., & Gammie, C. F. 2001, ApJ, 546, 980
Palau, A., Ballesteros-Paredes, J., Vázquez-Semadeni, E., et al. 2015, MNRAS, 453, 3785
Palau, A., Fuente, A., Girart, J. M., et al. 2013, ApJ, 762, 120
Press, W. H. (ed.) 2002, Numerical Recipes in C++: The Art of Scientific Computing (USA: Trelgol Publishing)
Qiu, K., Zhang, Q., Menten, K. M., et al. 2014, ApJL, 794, L18
Rahman, M., Matzner, C. D., & Moon, D.-S. 2013, ApJ, 766, 135
Remijan, A., Biggs, A., Cortes, P.A., et al. 2018, ALMA Cycle 6 Technical Handbook (ALMA Cycle 6 Technical Handbook) (ALMA Partnerhip)
Rivera-Ingraham, A., Martin, P. G., Polychroni, D., et al. 2013, ApJ, 766, 85
Robitaille, T., & Bressert, E. 2012, APLpy: Astronomical Plotting Library in Python, Astrophysics Source Code Library, ascl:1208.017
Sanhueza, P., Jackson, J. M., Zhang, Q., et al. 2017, ApJ, 841, 97
Saral, G., Audard, M., & Wang, Y. 2018, A&A, 620, A158
Schleuning, D. A. 1998, ApJ, 493, 811
Shu, F. H. 1992, Physics of Astrophysics, Vol. II (Mill Valley, CA: Univ. Science Books)
Spitzer, L. 1978, Physical Processes in the Interstellar Medium (New York: Wiley-Interscience), 333
Sridharan, T. K., Rao, R., Qiu, K., et al. 2014, ApJL, 783, L31
Tan, J. C., Beltrán, M. T., Caselli, P., et al. 2014, in Protostars and Planets VI, ed. H. Beuther (Tucson, AZ: Univ. Arizona Press), 149
Tang, K. S., Li, H.-B., & Lee, W.-K. 2018, ApJ, 862, 42
Tang, Y.-W., Ho, P. T. P., Girart, J. M., et al. 2009, ApJ, 695, 1399
Tobin, J. J., Hartmann, L., Bergin, E., et al. 2012, ApJ, 748, 16
Weidner, C., Bonnell, I. A., & Zinnecker, H. 2010, ApJ, 724, 1503
Zhang, B., Moscadelli, L., Sato, M., et al. 2014, ApJ, 781, 89
Zhang, Q., Wang, K., Lu, X., & Jiménez-Serra, I. 2015, ApJ, 804, 141
Zoonematkermani, S., Helfand, D. J., Becker, R. H., White, R. L., & Perley, R. A. 1990, ApJS, 74, 181